JGR Atmospheres

Key Points:
- Propagation and sources of inertia-gravity waves (IGWs) are investigated using the Gravity wave Regional Or Global RAy Tracer (GROGRAT)
- Orography, fronts, convection, and the flow imbalance including the jet stream are suggested as potential sources for the observed IGWs
- Relationships between the observed IGWs and their sources are examined

Supporting Information:
- Supporting Information S1

Correspondence to:
H.-Y. Chun,
chunhy@yonsei.ac.kr

Inertia-Gravity Waves Revealed in Radiosonde Data at Jang Bogo Station, Antarctica (74°37′S, 164°13′E): 2. Potential Sources and Their Relation to Inertia-Gravity Waves

J.-H. Yoo[1] (iD), **I.-S. Song[2]** (iD), **H.-Y. Chun[1]** (iD), and **B.-G. Song[2]** (iD)

[1]Department of Atmospheric Sciences, Yonsei University, Seoul, South Korea, [2]Division of Polar Climate Research, Korea Polar Research Institute, Incheon, South Korea

Abstract Potential sources of inertia-gravity waves (IGWs) in the lower stratosphere ($z = 15$–22 km) at Jang Bogo Station, Antarctica (74°37′S, 164°13′E) are investigated using 3-year (December 2014 to November 2017) radiosonde data, including the 25-month result (December 2014 to December 2016) analyzed in Yoo et al. (2018, https://doi.org/10.1029/2018JD029164, Part 1). For this investigation, three-dimensional backward ray tracing calculations are conducted using the Gravity wave Regional Or Global RAy Tracer. Among 248 IGWs, 112, 68, and 68 waves are generated in the troposphere ($z < 8$ km), tropopause ($z = 8$–15 km), and lower stratosphere ($z = 15$–18.5 km), respectively. These waves mainly propagate from the northwestern and southwestern regions of Jang Bogo Station dominated by the prevailing westerlies between the upper troposphere and lower stratosphere. Potential sources of IGWs are categorized into orography, fronts, convection, and the flow imbalance including the upper-tropospheric jet stream. In the troposphere, relatively large numbers of waves are associated with fronts (37) and orography (35) compared with convection (28). In the tropopause (stratosphere), 36 (42) waves, including 11 cases associated with the upper-tropospheric jet stream, are excited by the flow imbalance. Waves related to the flow imbalance are characterized by low intrinsic frequency (1–$2f$), short vertical wavelength (1–2 km), and longer horizontal wavelength (50–1000 km), whereas the waves induced by the tropospheric sources have wider ranges of intrinsic frequency (1–$20f$) and vertical wavelengths (1–15 km) with relatively shorter horizontal wavelengths (less than 500 km).

1. Introduction

The crucial roles of gravity waves (GWs) in shaping the dynamic and thermal structures of the middle atmosphere have long been recognized (Lindzen, 1981). Momentum fluxes (MFs) that GWs transport are deposited when they are dissipated, and GW drag (GWD) acts as a body force that induces the middle atmospheric circulation. Due to the short spatial scales of GWs that range from a few kilometers to several hundreds of kilometers, GWs cannot be fully resolved in the atmospheric general circulation models (GCMs), and thus, their impacts need to be represented through parameterizations (Kim et al., 2003). Recently, as GCMs generally extend into the middle atmosphere, accurate parameterizations of the GW effects have become more necessary (Plougonven et al., 2013). Over the last few decades, considerable progress has been made in the GWD parameterizations. However, inaccuracies in parameterized gravity wave momentum flux still cause uncertainties in large-scale atmospheric circulations in models (Geller et al., 2013). The cold-pole problem and excessively strong polar vortex in the Southern Hemisphere (SH) polar stratosphere in most GCMs are likely attributed to the lack of GWD, namely, the missing GWD in the SH polar latitudes (Garcia et al., 2017; McLandress et al., 2012), which is significantly important in inducing considerable downward control in the temperature from the mesosphere to the lower stratosphere (Garcia & Boville, 1994). This raises the importance of correcting inaccuracies in current parameterizations in a way that is tied to realistic physical constraints based on comprehensive observations and sophisticated simulations of GWs in the SH polar regions (Plougonven et al., 2017).

One of the main challenges in improving parameterizations of GWs concerns the different physical properties of GWs depending on the various wave sources. These parameterizations require not only detailed knowledge of the distribution and intermittency of the wave sources but also characteristics of GWs

depending on their sources. In general, GWs are generated by orography, frontal activities, convection, the jet stream, etc. (Fritts & Alexander, 2003; Kim et al., 2003, and references therein). In the SH, the Antarctic Peninsula, southern Andes, and Transantarctic Mountains play major roles in generating strong orographic GWs, as evidenced by aircraft, balloon-borne and satellite observations (Alexander & Teitelbaum, 2011; Baumgaertner & McDonald, 2007; Ern et al., 2004; Hertzog et al., 2008; Hoffmann et al., 2013; McLandress et al., 2000; Preusse et al., 2002; Vincent et al., 2007). In addition, the small mountainous islands scattered in the Southern Oceans (Alexander et al., 2009; Alexander & Grimsdell, 2013; Wu et al., 2006) and steep topography along the coastal lines of Antarctica (Watanabe et al., 2006; Wu & Jiang, 2002) have also been recognized as important sources of the orographic GWs. As the SH is largely covered by oceans, the importance of the nonorographic GW sources (including fronts, convection, and the jet stream) has also been emphasized in several previous studies (Ern et al., 2011; Hertzog et al., 2008; Plougonven et al., 2013; Vincent et al., 2007; Yan et al., 2010). Hendricks et al. (2014) elucidated that the nonorographic GWs contribute to the belt of large MFs in the stratosphere extending across the Southern Ocean from east of the Andes to south of New Zealand. More specifically, Eckermann and Vincent (1993) reported that enhancement of GW activity occurs in the vicinity of the surface front over southern Australia based on radar measurements. Yoshiki et al. (2004) suggested that the tropospheric disturbances in the upper troposphere enhance GW activities during early spring at Syowa station. Guest et al. (2000) identified inertia-gravity wave (IGW) production by the jet stream over Macquarie Island from radiosonde data and ray tracing analysis. Although cumulus convection is mainly active in the tropics, Choi and Chun (2013) showed that GWs generated by cumulus convection in SH storm tracks during winter can propagate poleward and significantly impact on the SH polar winter stratosphere.

In order to understand GW characteristics depending on the sources, it is important to correlate GWs with their sources. Ray tracing is a widely used method for tracking the propagation and evolution of GW characteristics and amplitude (Marks & Eckermann, 1995). Backward ray tracing allows for identifying GW sources and correlating the properties of GWs (e.g., wavelengths and phase velocities) with their potential sources, which is crucial for constraining GW parameterizations in models. Several studies have conducted ray tracing analyses to identify the sources of GWs observed in the stratosphere using radiosonde and lidar data (Chun et al., 2007a; Guest et al., 2000; Hertzog et al., 2001; Ki & Chun, 2010; Ki & Chun, 2011; Pramitha et al., 2015, 2016).

Recently, Yoo et al. (2018, hereafter Part 1) analyzed IGWs in the troposphere and lower stratosphere revealed in radiosonde observations at Jang Bogo Station (JBS; 74°37′S, 164°13′E) for 25 months (December 2014 to December 2016). In Part 1, characteristics, energy, and MF of IGWs have been obtained using the Stokes parameter and rotary spectrum methods. Given that near-inertial frequency waves, which are mainly detected from radiosondes, can propagate long horizontal distances from their source regions for a long duration, the ray tracing approach is particularly important for IGWs to identify their sources (Ki & Chun, 2011). Several previous studies have analyzed the characteristics of GWs using radiosonde observations in the SH polar regions (Part 1, and references therein); however, there are little studies that correlate the observed GWs and their potential sources using the ray tracing method in that region.

Therefore, as a continuing work of the companion study (Part 1), we investigate the potential sources of IGWs in the lower stratosphere over JBS in Antarctica using 3-year (December 2014 to November 2017) radiosonde data, including the 25-month (December 2014 to December 2016) result analyzed in Part 1. With the IGW characteristics extracted from radiosonde data, ray tracing analyses are carried out using a three-dimensional ray tracing model, Gravity Wave Regional Or Global RAy Tracer (GROGRAT) (Mark & Eckermann, 1995; Eckermann & Marks, 1997), to investigate the propagation properties and to identify the location of the potential sources. Based on the ray tracing analysis, we categorize the potential sources of the observed IGWs as orography, fronts, convection, and the flow imbalance including the upper-tropospheric jet stream. In addition, the fifth-generation reanalysis data released from the European Centre for Medium Range Weather Forecasts (ECMWF) ERA5 reanalysis data are employed to examine GWs associated with the aforementioned sources. By classifying the observed IGWs into the potential sources, we examine relationships between the GW characteristics and their sources in detail, including the intermittency, intrinsic frequency, wavelengths, and phase velocities.

The paper is organized as follows: characteristics of IGWs obtained from 3-year radiosonde data are briefly described, and the backward ray tracing analysis method is introduced in section 2. In section 3, the identification methods for each source are discussed, and the representative GW cases associated with each source revealed in the high-resolution ERA5 data are presented. In section 4, the observed IGWs are categorized into potential sources, and relationships between GWs and their sources are examined. A summary and conclusions are given in section 5.

2. Data and Analysis Methods

In the present study, we use the radiosonde data collected at JBS during a 3-year period from December 2014 to November 2017: 11-month radiosonde data (from January 2017 to November 2017) are added following the 25-month radiosonde observations analyzed in Part 1 (from December 2014 to December 2016). Details of radiosonde data are provided in Part 1, but some brief information will be given here. Observations were made once a day using a Vaisala RS92G radiosonde. Temperature and wind speed were recorded every 2 s, corresponding to a vertical resolution of 10–12 m, given that the ascending speed of the balloon was approximately 5–6 m s^{-1}. Due to the irregular vertical spacing of the temperature and wind speed, the original profiles are uniformly interpolated with an interval of 20 m using the cubic spline method. Additionally, a 200-m moving average is applied to the interpolated data to reduce the observational errors (Part 1).

2.1. Characteristics of IGWs

In this study, we focus on IGWs observed in the lower stratosphere in the altitudinal region of 15–22 km, as in Part 1. Hence, among a total of 1,006 profiles launched at JBS for 3 years, 806 (80%) soundings, which ascended to the height of 22 km, are used.

Following the methods described in Part 1, the GW components are defined as the wind and temperature perturbations (u', v', and T'), which are obtained by subtracting the basic-state profiles ($\overline{u}$, $\overline{v}$, and $\overline{T}$) from the observed profiles. The basic-state profile is determined as the third-order polynomial fit of the original profile in the altitudinal region of 15–22 km. In the present study, only the coherent perturbations that satisfy the following two conditions are analyzed: (i) the degree of polarization (dp) is greater than 0.5 and (ii) the intrinsic frequency ($\hat{\omega}$) is in a range of 1.1–10f, where f is the magnitude of Coriolis parameter. Out of 806 profiles, 547 (67%) soundings are identified as coherent IGWs and used for the analysis.

Characteristics of IGWs, including the vertical wavenumber (m), intrinsic frequency ($\hat{\omega}$), horizontal wavenumber (k_h), and phase and group velocities, are examined from each sounding. The vertical wavenumber m is calculated using the vertical Fourier components of the perturbations of zonal and meridional winds. The intrinsic frequency divided by the Coriolis parameter ($\hat{\omega}/f$) can be obtained from the axial ratio of the horizontal wind perturbation hodograph (u' and v') using the Stokes parameter method. For given m and $\hat{\omega}$, the horizontal wavenumber k_h is obtained from the dispersion relationship of IGWs. The intrinsic phase velocity ($\hat{c}$), ground-based phase velocity (c), and ground-based group velocity (c_g) are calculated using $\hat{\omega}$, k_h, and the vertically averaged basic-state horizontal wind vector over the stratospheric analysis layer. Kinetic energy (E_K) and potential energy (E_P) of GWs are obtained using the perturbations of horizontal wind velocity and temperature, respectively. Details of calculations of the wave parameters are described in Part 1.

Figure 1a shows the intrinsic frequency divided by the Coriolis parameter $\hat{\omega}/f$, vertical wavelength λ_z, horizontal wavelength λ_h, kinetic energy E_K, and potential energy E_P of the observed IGWs. The numbers written in the upper-right corner of each panel denote the average values regardless of the vertical propagation direction (black), for the up-going IGWs (red), and for the down-going IGWs (blue). The gray vertical line represents the initial date of the additional observations extending the data used in Part 1. Figure S1 in the supporting information presents the zonal and meridional winds and Brunt-Väisälä frequency averaged in the stratospheric analysis layer used for the calculation of IGW parameters. Note that the number of the observed IGWs during the winter months (June, July, and August, JJA) is much smaller than that in other seasons (Table 2 in Part 1), as the balloons burst before they reach the upper limit (22 km) of the stratospheric analysis layer due to the reduced elasticity by the extremely low temperature in winter (Figure 3 in Part 1).
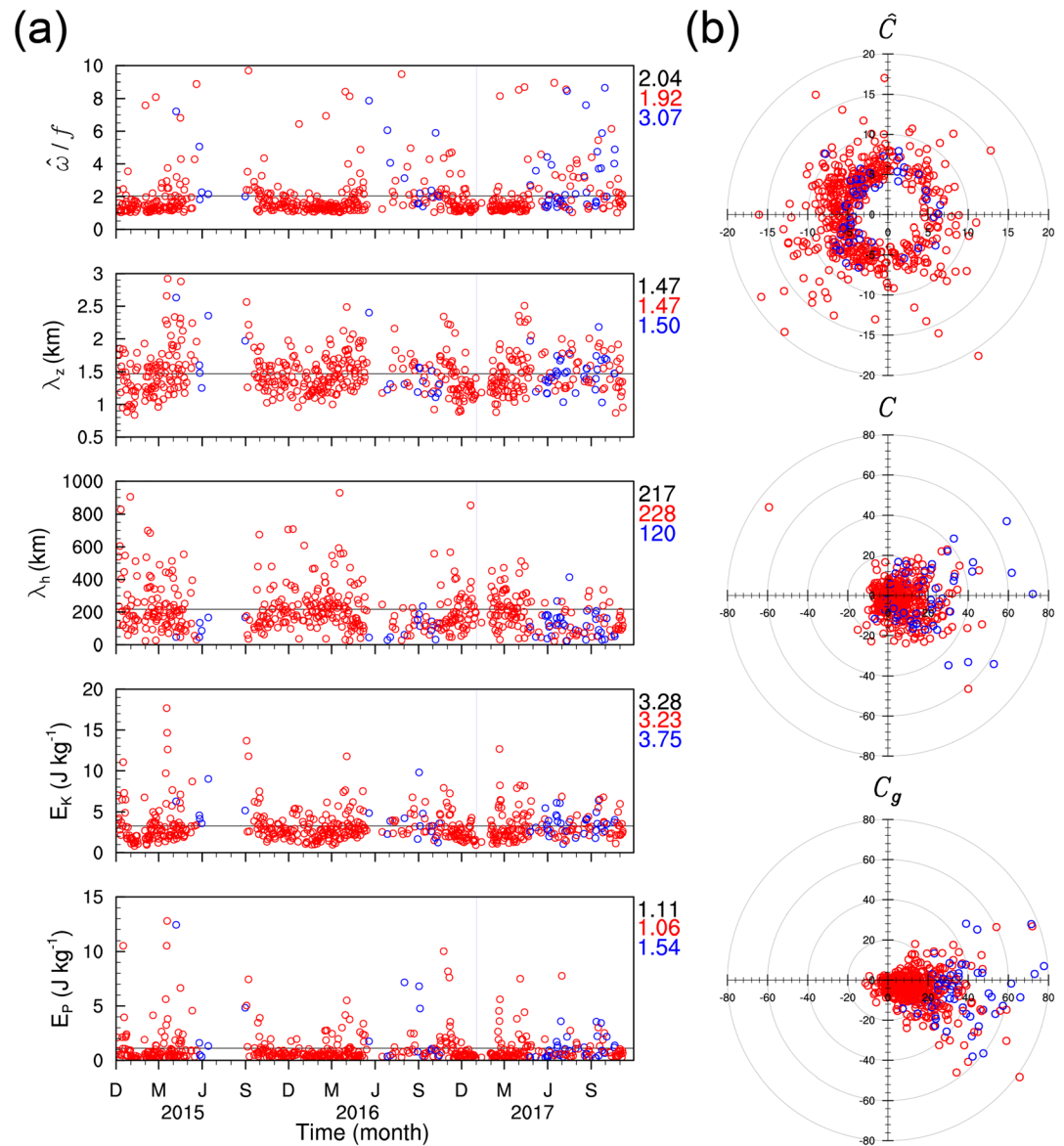
Figure 1. (a) Scatter plots of the intrinsic frequency divided by the Coriolis parameter (first row), vertical wavelength (second row), horizontal wavelength (third row), kinetic energy per unit mass (fourth row), and potential energy per unit mass (fifth row) calculated for each wave in the stratosphere. The black lines across the graphs represent the averages for each value regardless of the vertical propagation direction. The red and blue circles denote upward and downward propagating waves, respectively. Average values for all, upward, and downward propagating waves are written in black, red, and blue, respectively, on the upper right side of each panel. The gray vertical line represents the initial date of the additional observations that extend the data used in Part 1. (b) Distributions of the intrinsic phase velocity (first row), ground-based phase velocity (second row), and ground-based group velocity (third row) for each wave in the stratosphere. Right and upward directions indicate eastward and northward directions, respectively.

As identified in Part 1 (Figure 8 therein), up-going IGWs are predominant, while down-going IGWs appear in wintertime, primarily from May to October. For the down-going IGWs, the polar night jet in the winter stratosphere has been suggested as a potential source (Figure 9 in Part 1, and references therein). The seasonal preference in the down-going IGWs becomes more obvious over the extended period (January 2017 to December 2017) considered in the present study, as the number of the observed IGWs increases during the wintertime. The average intrinsic frequency for all waves is 2.04f corresponding to a period of 6.11 hr. Typical short vertical wavelengths appear with an average value of 1.47 km. The horizontal wavelengths

of each wave calculated from the dispersion relation are less than 1,000 km, with an average of 217 km. In the extended period, the intrinsic frequencies exhibit somewhat higher values, but vertical wavelengths are similar to those in the previous period. As a result, the horizontal wavelengths have relatively lower values in the extended period. The average kinetic and potential energies are 3.28 and 1.11 J kg^{-1}, respectively. The kinetic energies somewhat increase in the extended period, while the potential energies are similar to those in the previous period. The intrinsic frequencies and vertical wavelengths exhibit seasonal variations that increase from autumn (March, April, and May, MAM) to spring (September, October, and November, SON) with a few exceptionally higher values. The corresponding horizontal wavelengths decrease (increase) significantly from March to September (October to February).

Figure 1b shows the distributions of the intrinsic phase velocity, ground-based phase velocity, and ground-based group velocity. Both up-going and down-going IGWs generally have westward intrinsic phase velocities with a speed range of 4–8 m s^{-1}, whereas the ground-based phase and group velocities are predominantly eastward with a maximum speed of 80 m s^{-1} in September. As the background winds become large in winter (JJA) and spring (SON) (Figure S1), strong seasonal variations are observed in the ground-based phase and group velocities (Figure S2). In summer (December, January, and February, DJF), the ground-based phase velocities show a nearly isotropic distribution with speeds less than 25 m s^{-1}, whereas those in autumn (MAM) are directed more southeastward with increase in speeds. In winter (JJA) and spring (SON), both ground-based phase and group velocities are mostly directed northeast and southeastward with a maximum speed of nearly 70 m s^{-1} (50 m s^{-1}) for down-going (up-going) IGWs.

2.2. Backward Ray Tracing Analysis

To investigate the propagation and sources of the up-going IGWs, a backward ray tracing analysis is conducted using a version of GROGRAT that includes the Earth's curvature effect (Hasha et al., 2008; Kalisch et al., 2014). Details on the ray tracing equations are described in Appendix A. In the present study, the basic-state wind, stability, and scale-height required for ray tracing calculations are obtained using the 6-hourly ECMWF Interim reanalysis (ERA-Interim) data (Dee et al., 2011) with a horizontal resolution of $1.5° \times 1.5°$ in longitude and latitude and 37 pressure levels from 1,000 to 1 hPa. Considering that the background atmosphere should exhibit all synoptic-scale structures without finer-scale GWs (Preusse et al., 2014), the background wind and temperature are interpolated to a coarser grid with a resolution of 2.5° latitude and 3.75° longitude on 22 pressure levels corresponding to an altitude spacing of 2.5 km. In this study, we use snapshots of the background atmospheres when the IGWs were observed, ignoring the temporal variations in the background wind, stability, and scale-height in the ray tracing calculation. Consequently, the ground-based frequency ω is invariant following the rays.

The wave parameters $(k, l, \hat{\omega})$ estimated from the radiosonde soundings (section 2.1) and m calculated from the dispersion relationship for the estimated k, l, and $\hat{\omega}$ are used as the initial parameters for the ray tracing calculation. Criteria for terminating the ray calculation are discussed as follows: (1) When a ray passes through the physical domain ranges from 87.5°S to 87.5°N or reaches the ground, (2) when the vertical WKB condition is violated with the value of a parameter, defined as $\delta = (1/m^2)|\partial m/\partial z|$, sufficiently greater than 1 (here, $\delta = 2$ is used, which occurs as $m^2 \to 0$), (3) when IGWs become evanescent ($m^2 \leq 0$), and (4) when the vertical group velocity c_{gz} falls below 0.001 m s^{-1}, which means that the wave is approaching a critical level. Regarding the threshold value of c_{gz}, Lin and Zhang (2008) and Evan et al. (2012) used 0.0001 m s^{-1}, whereas Ki and Chun (2011) and Chun et al. (2007) used 0.001 and 0.01 m s^{-1}, respectively. The result of backward ray tracing with the threshold of 0.001 m s^{-1} is not significantly different from that with the threshold of 0.0001 m s^{-1}, whereas in the case of 0.01 m s^{-1}, rays tend to be terminated more quickly. Hence, following Ki and Chun (2011), the threshold of c_{gz} is determined as 0.001 m s^{-1}. Because some rays propagate for an unrealistically long time, we additionally force the rays to be terminated (5) when the total integration time exceeds 120 hr.

Because the radiosonde data have observational errors, the wave parameters estimated from the soundings could contain inherent uncertainties. Given that the ray tracing calculation is sensitive to the initial values of each ray, we perform a sensitivity test to evaluate whether the uncertainties in each parameter significantly influence the calculation result. Following Ki and Chun (2011), we construct a set of 125 rays for each

sounding containing all possible combinations of initial wave parameters $(k_0, l_0, \widehat{\omega}_0)$, calculated by adding uncertainties of $\pm 1\%$ and $\pm 3\%$ to the wave parameters $(k, l, \widehat{\omega})$ estimated from radiosonde observations:

$$k_0 = k \pm 0.01k \times n, \qquad n = 0, 1, 3 \tag{1}$$

$$l_0 = l \pm 0.01l \times n, \qquad n = 0, 1, 3 \tag{2}$$

$$\widehat{\omega}_0 = \widehat{\omega} \pm 0.01\widehat{\omega} \times n. \qquad n = 0, 1, 3 \tag{3}$$

The initial vertical wavenumber m_0 is calculated using the dispersion relation of IGWs in equation A3 for given $k_0, l_0,$ and $\widehat{\omega}_0$.

There are also some uncertainties related to the initial position of the ray tracing. As seen in Figure 2 of Part 1, balloons drift horizontally with the background winds during their ascents, implying that the horizontal location at which the wave is observed in the lower stratosphere is different from that of the station. However, it was found that changes in the initial horizontal positions, taking into account the horizontal drift of the balloons during their ascent in the stratospheric analysis layer, do not significantly change the trajectories of rays (not shown). On the other hand, variations in the initial launching altitude tend to cause some differences in the ray trajectories. However, for simplicity, we determine the initial altitude as 18.5 km, which is the center of the stratospheric analysis layer (15–22 km). Therefore, a set of 125 rays containing the arbitrary errors given by equations 1–3 on the observed wave parameters are integrated backward simultaneously with a time interval of 0.2 hr from the horizontal location of JBS and an altitude of 18.5 km. Then, we select the "convergence cases", which are defined as follows: More than 70% of 125 rays (87 rays) should be terminated within (1) a given horizontal area (the spherical area corresponding to the area of a circle with radius R of the distance of 3° in latitude) and (2) a vertical range ($z = \pm 2$ km) from the termination position of the ray with the original wave parameters $(k, l, \widehat{\omega})$. In the present study, only 248 waves among the 480 observed IGWs satisfy the convergence criteria and they are used to investigate the propagation properties and potential sources.

Figure 2 presents the geographical locations of the termination positions and backward trajectories of each ray, categorized by the cases traced down to the troposphere ($z < 8$ km), tropopause ($z = 8$–15 km), and stratosphere ($z = 15$–18.5 km). The altitude ranges of the three analysis layers are determined considering the seasonal variations in the tropopause height at JBS, which varies from 8 km in summer to 12 km in winter (Figure 6 in Part 1). Different colors of the ray back trajectories represent the corresponding altitude at the horizontal locations of each ray.

Out of 248 total waves, approximately 45% (112 waves) of the IGWs are traceable to the troposphere, whereas 27.5% (68 waves) and 27.5% of the waves are traced down to the tropopause and stratosphere, respectively. The majority of rays propagate roughly westward until they are terminated, implying that the propagations of the observed IGWs are affected by the prevailing westerlies from the upper troposphere to the lower stratosphere. Most of the termination positions (Figure 2a) in the troposphere (red crosses) are located in the longitudinal region of 90°E to 180° over the Southern Indian Ocean (70–45°S) as well as above the Antarctic continent and Ross Sea. On the other hand, the termination positions in the tropopause (green crosses) and stratosphere (blue crosses) are widely distributed across all longitudinal regions in the southern latitudes poleward of 50°S. Many of the termination locations above the Southern Indian Ocean coincide with a broad band of significantly elevated wave variances associated with the nonorographic GW sources in Figure 1 of Hendricks et al. (2014). As inferred from the termination positions in Figure 2a, most of the rays that penetrate the troposphere propagate relatively shorter horizontal distances (Figure 2b), whereas many of the rays terminated in the tropopause and stratosphere propagate long horizontal distances from their potential source regions to the observation station (Figures 2c and 2d). It is also noticeable that many of the rays traced down to the troposphere predominantly travel horizontally in between the tropopause and stratosphere after a rapid vertical propagation from their termination altitude to the tropopause (Figure 2b). Enhancement (reduction) in the upward propagation from the troposphere to the tropopause (from the tropopause to the stratosphere) occurs as the vertical group velocity increases (decreases) through an increase (decrease) in the vertical wavenumber. This is explained by both the decrease (increase) in the Brunt-Väisälä frequency and increase (decrease) in the background wind projected to the wavenumber vector (will be discussed in detail in section 4).
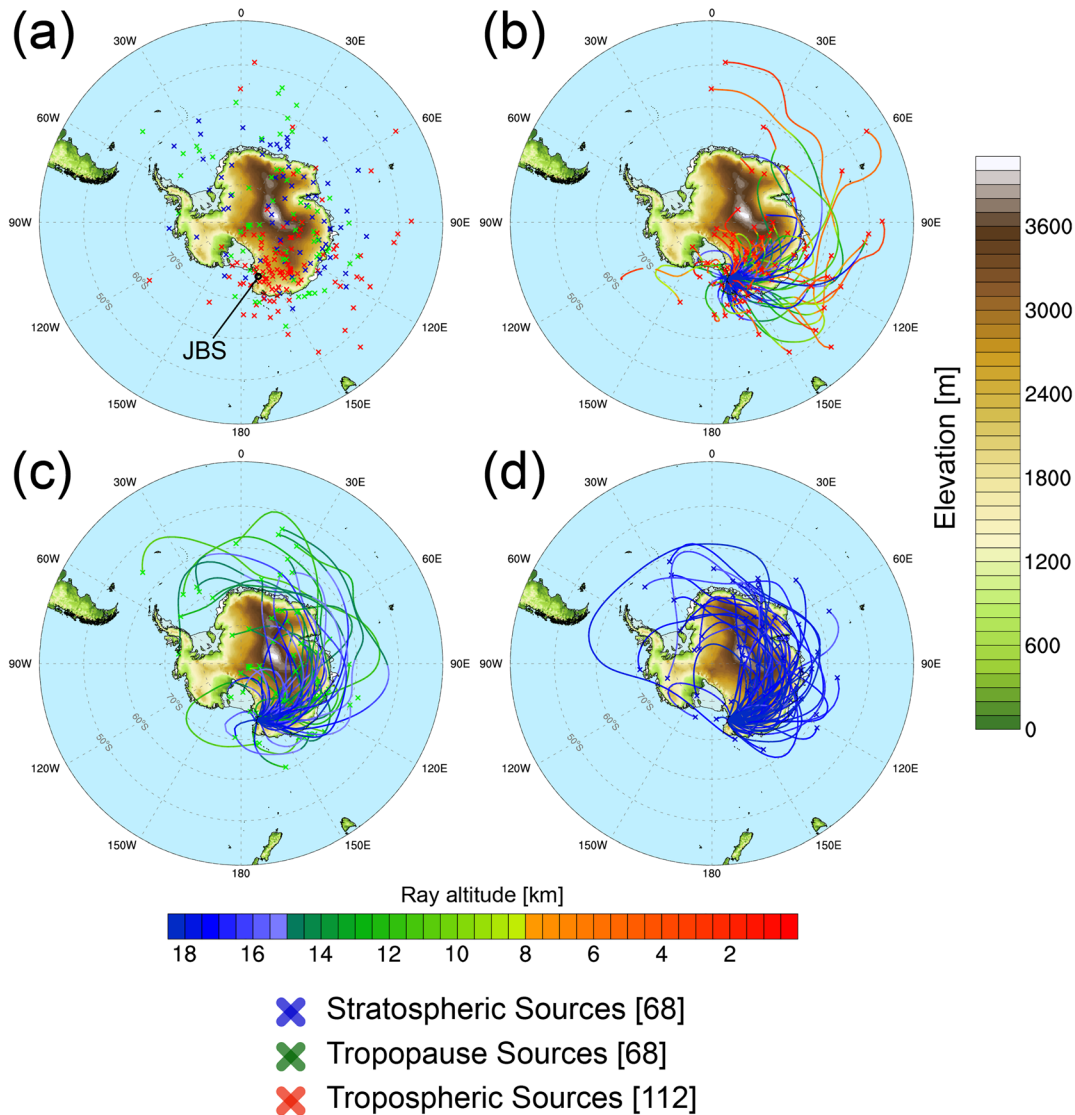
Figure 2. (a) Geographical distribution of the termination positions of the rays traced down to the troposphere (red cross), tropopause (green cross), and strato-sphere (blue cross). Back trajectories of the rays terminated in the (b) troposphere, (c) tropopause, and (d) stratosphere. The numbers in brackets are the number of rays terminated in each layer. The colors of each line represent the corresponding altitude of the rays at the horizontal location.

3. Identification Methods for the Potential Sources

The observed IGWs can be generated by various sources, such as flows over mountains, fronts, convection, and the jet stream. It is of importance to distinguish the GW sources to determine the respective roles of GWs in depositing the momentum in the middle atmosphere (Hertzog et al., 2008). Therefore, we categorize the potential sources of IGWs using the reverse ray tracing approach. In this study, the termination position is considered to be the wave generation location, although the waves could have been emitted anywhere along the raypath as well as the termination position. In this section, we will introduce the method to categorize the potential sources of IGWs in detail, including the diagnostic layers, indices, and their threshold values.

Figure 3 represents the decomposition of the analysis layer (from the surface to the ray start altitude) into the potential source regions of IGWs. We decompose the atmosphere into three vertical layers, the troposphere (0–8 km), tropopause (8–15 km), and stratosphere (15–18.5 km) and suggest the probable GW sources in each layer as follows: orography, fronts, convection, and the flow imbalance including the tropopause jet stream. In the troposphere, severe Transantarctic Mountains and steep slopes in mainland Antarctica can excite mountain waves. Considering that the maximum terrain height of Antarctica reaches 4 km
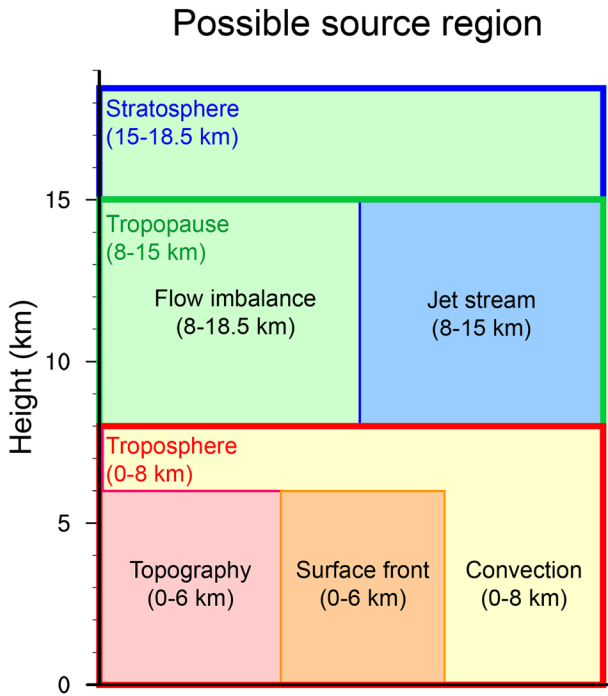
Possible source region

Figure 3. Vertical locations of the potential sources of IGWs.

(Figure S3), the diagnostic layer for orographic GWs is determined as 0–6 km, allowing the possibility that GWs can emerge somewhat above the topography. The altitudinal region for examining the generation of GWs by fronts is determined the same as that of orographic GWs, because we mainly consider the lower-tropospheric fronts. For convective GWs, their generation is diagnosed in the whole tropospheric layer (0–8 km), allowing the possibility that convection can reach the tropopause height, although the 30-year climatology of the convective cloud top pressure from the Climate Forecast System Version 2 (Saha et al., 2014) reanalysis data exhibits a maximum frequency at approximately 600 hPa in the latitudes of 45–70°S (not shown). In the tropopause and stratospheric layer (8–18.5 km), we focus on the generation of GWs associated with the flow imbalance. In the tropopause layer, we further examine whether the flow imbalance is associated with the upper-tropospheric jet stream. Considering the inherent uncertainties in the location and time of ray termination, the potential sources are investigated within the same horizontal and vertical area (hereafter referred to as the diagnostic area) where the sensitivity tests in section 2.1 are conducted, within 3 hr around the termination time. The diagnostic method for each source is written in Table 1. Detailed explanations will be given below with the five representative source cases.

In addition, we briefly assess whether the GWs associated with the particular sources actually appear for the representative cases. Several previous studies have conducted mesoscale numerical simulations not only to estimate characteristics of GWs in support of observations but also to more precisely understand the generation mechanisms of GWs associated with larger spatial-scale atmospheric phenomena. Spiga et al. (2008) performed mesoscale simulations using the Weather Research Forecast model to reproduce the GWs observed from radiosonde and remote satellite above the Andes Cordillera region and suggested four likely sources (the upper-tropospheric jet stream, lower-tropospheric fronts, convection, and topography) for the observed GWs with probable emission processes. ERA5 is the fifth-generation reanalysis released from the ECMWF (Hersbach & Dee, 2016), which is significantly improved upon the ERA-Interim data as they have much higher spatial and temporal resolutions. ERA5 analyses are produced using the ECMWF Integrated Forecast System with a horizontal resolution of ~31 km (T_L639 spectral grid) on 137 hybrid sigma-pressure levels in the vertical direction, with a top level of 0.01 hPa (~80-km altitude). This allows for a better representation of small-scale GWs, as reported in Hoffmann et al. (2019), without performing mesoscale numerical simulations. Therefore, in this study, we employ ERA5 to examine the existence of GW signals associated with the potential sources for some representative cases.

In the analysis of ERA5 data, GWs are determined as the vertical wind perturbations, which are obtained by subtracting the large-scale background field from the original vertical wind. The background field is defined at each grid point and time by calculating the running average over the spherical area bounded by the distance of 3° in latitude (approximately 333 km) from each grid point, which is comparable to the area of the 300 km radius used in the previous study Kim et al. (2016). Because ERA5 data provided by ECMWF have a horizontal resolution of 0.25° on the vertical resolution of 37 levels (1,000–1 hPa), the minimum resolvable horizontal and vertical wavelengths of GWs are approximately limited to 120 and 1–3 km, respectively.

3.1. Identification of the Orographic Source
3.1.1. Diagnostic Method

Orography is known as an important GW source, given that orographically induced GWs have a typical characteristic that a ground-based phase speed is 0, and thus, their dissipation acts as a significant force

Table 1

Diagnostic Methods Used to Identify the Potential Sources of the IGWs Within a Given Horizontal (the Spherical Area Corresponding to the Area of a Circle With Radius R Equivalent to a Distance of 3° in Latitude) and Vertical Area (z = ±2 km) From the Termination Position at the Nearest Time

	Source	Diagnostic method
i	Orography	i Slope of the topography > 5 m km^{-1} ii Gravity wave phase velocity < 10 m s^{-1}
ii	Surface front	$FF \geq 0.1$ K^2 (100 km)$^{-2}$ hr^{-1}
iii	Convection	Hourly precipitation ≥ 2.5 mm hr^{-1}
iv	Flow imbalance	$|RNBE| \geq 1.5 \times 10^{-9}$ s^{-2}
v	Jet stream	i $|RNBE| \geq 1.5 \times 10^{-9}$ s^{-2} ii Wind speed > 20 m s^{-1}

decelerating the winter tropospheric and stratospheric jets. As mentioned in the introduction, along with mountainous regions including the Antarctic Peninsula and Transantarctic Mountains, intense GW activities are also identified along the coastal areas of the Antarctic Continent from the high-resolution GCM simulation (Watanabe et al., 2006) as well as Upper Atmosphere Research Satellite Microwave Limb Sounder observations (Wu & Jiang, 2002).

Based on these previous studies, Vincent et al. (2007) decomposed the SH regions into orographic and non-orographic GW fields using the topography gradient calculated from the NOAA 5′× 5′ gridded elevation data. In their study, $5° \times 20°$ longitude-latitude bins for which the mean of the upper 10% of the topographic gradients exceeds a threshold value of 15 m km^{-1} were flagged as orographic source regions. Following Vincent et al. (2007), we set criteria to examine the excitation of orographic GWs: Among the waves of which ray is terminated in the layer of 0–6 km (Figure 3), when (i) the slope of the topographic elevation calculated from the 1-arc-min global relief model (ETOPO1) elevation data (Amante & Eakins, 2009) exceeds a threshold value of 5 m km^{-1} within the diagnostic area and (ii) the ground-based horizontal phase velocity of GWs at the termination location is less than 10 m s^{-1}, the GW is classified as the wave generated by the orography (Table 1, i). Reduction of the threshold value from 15 to 5 m km^{-1} is determined from the visual comparison of our elevation slope (Figure S3b) with the orographic source region defined in the previous study (see Figure 3 of Vincent et al., 2007). Note that the direction of the surface wind with respect to mountains can be an important fact to diagnose mountain waves (e.g., Alexander et al., 2013). For all the mountain wave cases selected in the current study by the conditions of ground-based phase velocity and orographic slopes, there were no cases of which the directions of the horizontal surface winds blew parallel to the significant orographic slopes inside the diagnostic area. Accordingly, we did not include a criterion of surface wind direction for the orographic GWs.

3.1.2. A Case of the Orographic Source

Figure 4 presents a case categorized into the orographic GW. Figure 4a describes the ray back trajectory and the information of the location and time of observation and generation of the wave. This IGW was observed in the radiosonde sounding launched at 00 UTC on 16 January 2016. Backward ray tracing of the wave is terminated at 2.16-km altitude at 76.04°S and 164.72°E near JBS. The total integration time is approximately 116 hr, indicating that the wave emanated at approximately 04 UTC on 11 January 2016. Figure 4b shows the orographic slope and near surface horizontal wind vector at 850 hPa from the ERA-Interim reanalysis data at 04 UTC on 11 January 2016 in the zoomed map of the fan-shaped area in Figure 4a. Within the diagnostic area marked by black circles, there are intense gradients of orography greater than 15 m km^{-1} along the west coast of the Ross Sea. In addition, the near-surface wind flows nearly perpendicular to the steep orography on the west coast of the Ross Sea at a speed of approximately 15 m s^{-1}, which is favorable for generating orographic GWs. The ground-based phase velocity of this IGW at the termination position was 3.5 m s^{-1}. Note that a front is not suggested as the potential source, as we rule out the existence of frontal activities above a significant elevation slope greater than 15 m km^{-1} (will be discussed in section 3.2). In addition, no pronounced convective activity is identified in this region (not shown).

As mentioned previously in section 2, the vertical wind perturbations are used to investigate the possible orographic GW generation taking place within the diagnostic area. Figure 4c illustrates the perturbation of vertical wind with the horizontal wind vectors from ERA5 at 600 hPa (just above the maximum terrain height in the diagnostic area) at 04 UTC on 11 January 2016. Inside the diagnostic area marked by a black circle, a clear wave signature is identified in the downstream region (72–74°S and 160–170°E) of the dominant easterlies, which travel up the intense gradient of orography. This supports the diagnostic result in Figure 4b that the flow over the steep orography is responsible for the GW emission. Finally, we check the consistency of the GW property identified both in ERA5 and GROGRAT. For the comparison, the ensemble spread of the characteristics of GWs converged in the diagnostic area are considered, and the results are presented in Figure S6. First, the horizontal wavelength estimated from the vertical wind perturbation is approximately 100–125 km, which is somewhat longer than the horizontal wavelengths of 25–65 km calculated from GROGRAT (Figure S6a). However, the agreement between GROGRAT and ERA5 analysis does not extend to the vertical wavelength as the vertical resolution of the ERA5 is too coarse, and therefore, the vertical wavelength of the wave revealed in ERA5 is overestimated by a factor 4 compared to that of the wave from GROGRAT (not shown). The vertical wind perturbations in ERA 5 reveal dominant northwestward wave vector, which is different to the southwestward and southeastward wave vectors estimated from GROGRAT (Figure S6a). In
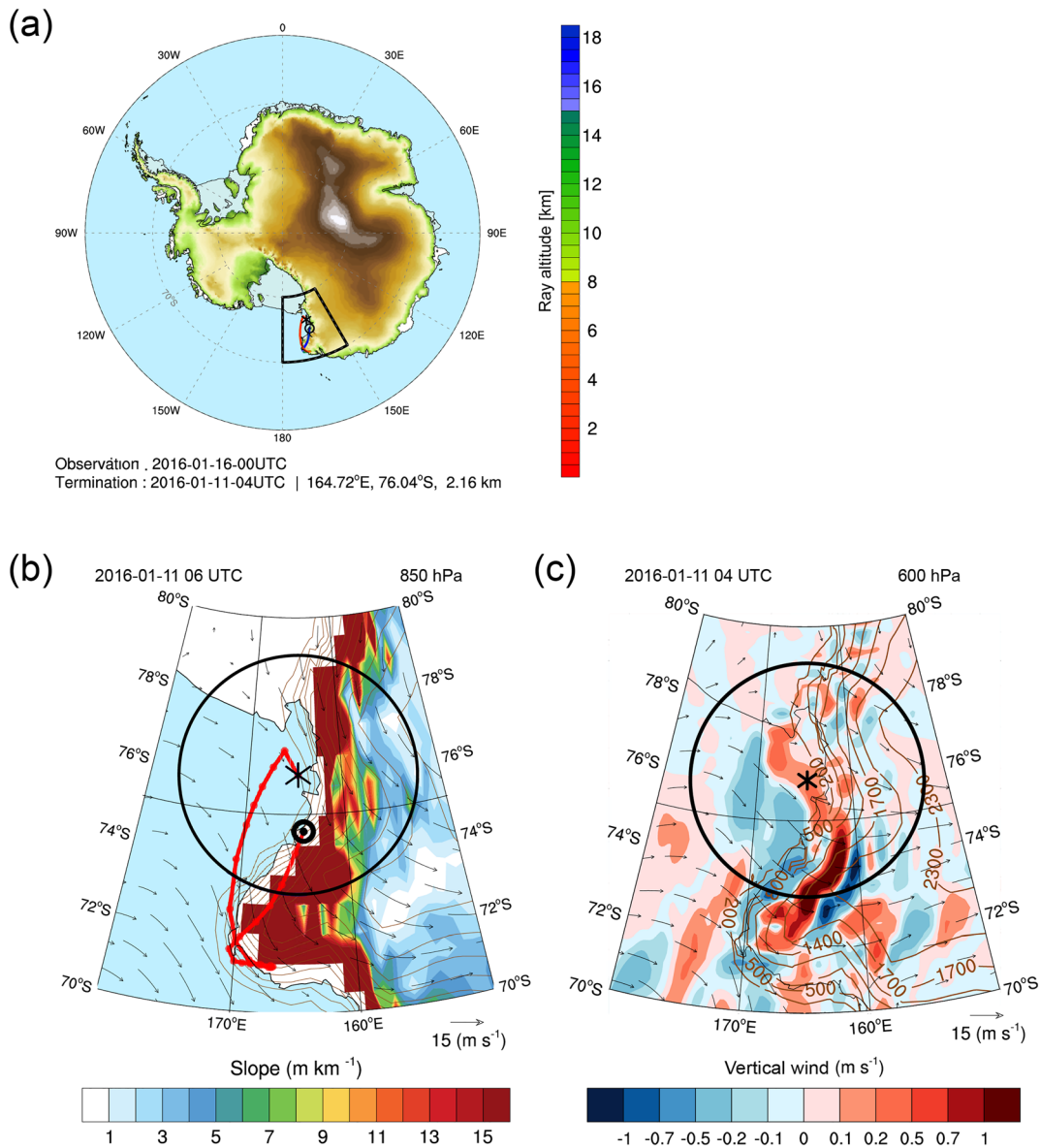
Figure 4. (a) Ray back trajectory of the IGW observed on 16 January 2016. The start and termination positions of the ray are marked with black double circles and asterisks, respectively. (b) Zoomed map of the black fan-shaped area in (a). The ray back trajectory (red line) of the IGW is superimposed on the topography elevation (brown line), slope (shading), and 850-hPa wind (arrow) at 06 UTC on 11 January 2016. The black circle represents the spherical diagnostic area corresponding to the area of a circle with the radius *R* of 3° latitude from the termination position. (c) Vertical wind velocity perturbation (shading) at 600 hPa with the horizontal wind vector (arrow) at 04 UTC on 11 January 2016.

conclusion, ERA5 seems to well represent the GW emission associated with orography, although it cannot precisely reproduce all the detailed quantitative properties of GWs. Nevertheless, it is thought to be a useful complementary tool to obtain insights into the generation and characteristics of GWs.

3.2. Identification of a Front Source
3.2.1. Diagnostic Method

Given that frontal activities frequently occur in the latitudinal belt of 40–60°S (polar front; Simmonds et al., 2012) over the Southern Ocean, the frontal system can be a plausible source for the observed GWs. Through high-resolution numerical simulations and ray tracing analysis, Griffiths and Reeder (1996) and Reeder and Griffiths (1996) showed that the cross-front ageostrophic circulation accompanying

frontogenesis is responsible for the generation of the stratospheric IGW. Charron and Manzini (2002) established the frontal GW parameterization by linking the emission of GWs to the condition of tropospheric flow that is favorable for frontogenesis using the frontogenesis function (FF; Miller, 1948; Hoskins, 1982) defined as follows:

$$FF = \frac{1}{2}\frac{D|\nabla\theta|^2}{Dt} = -\left(\frac{1}{a\cos\phi}\frac{\partial\theta}{\partial\lambda}\right)^2\left[\frac{1}{a\cos\phi}\frac{\partial u}{\partial\lambda} - \frac{v\tan\phi}{a}\right] - \left(\frac{1}{a}\frac{\partial\theta}{\partial\phi}\right)^2\left[\frac{1}{a}\frac{\partial v}{\partial\phi}\right] - \left(\frac{1}{a\cos\phi}\frac{\partial\theta}{\partial\lambda}\right)\left(\frac{1}{a}\frac{\partial\theta}{\partial\phi}\right) \quad (4)$$

$$\times\left[\frac{1}{a\cos\phi}\frac{\partial v}{\partial\lambda} + \frac{1}{a}\frac{\partial u}{\partial\phi} + \frac{u\tan\phi}{a}\right]$$

Here, θ is the potential temperature, u and v are zonal and meridional winds, respectively, and λ, ϕ, and a are the longitude, latitude, and mean radius of the Earth, respectively. Following the previous studies, we adopt FF as an indicator for diagnosing the frontal GWs. Diagnosis of the frontal GWs can be performed at a single level or layer. Charron and Manzini (2002) and Richter et al. (2010) chose a single level of 600 hPa (approximately 4.5-km altitude) as the diagnostic level of the frontal regions in GCM to parameterize the frontal GWs, given that the typical steering level of a front is located at approximately 600 hPa. On the other hand, Kim et al. (2016) calculated FF at all levels where GWs appeared to assess the ability of FF to diagnose the generation of frontal GWs. For the present study, an FF calculated at a single level is not sufficient to diagnose the wave generation by a front due to the deep analysis layer of 0–6 km. Therefore, we use FF calculated at all pressure levels within 2 km from the termination altitude to identify the frontal GWs.

Regarding the threshold value of FF, Charron and Manzini (2002) used 0.1 K^2 (100 km)$^{-2}$ hr^{-1}, whereas slightly lower values are used in other previous studies (e.g., 0.045 K^2 (100 km)$^{-2}$ hr^{-1} in Choi et al., 2018; Chun et al., 2019; Richter et al., 2010; 0.07 K^2 (100 km)$^{-2}$ hr^{-1} in Griffiths & Reeder, 1996) for the purpose of frontal GW parameterizations. To determine the threshold value, we visually compare maps of frontal regions at 850 hPa identified by the various thresholds (0.045, 0.07, and 0.1 K^2 (100 km)$^{-2}$ hr^{-1}) for FF and the 850-hPa sea level pressure in Figure S4 using ERA-Interim data gridded at 0.75° × 0.75° (lat. × lon.). As the threshold varies from 0.045 to 0.1 K^2 (100 km)$^{-2}$ hr^{-1}, many areas that are not considered coherent fronts disappear, and the threshold of 0.1 K^2 (100 km)$^{-2}$ hr^{-1} most closely matches the hand-analyzed surface maps made by the Australian government bureau of meteorology (Figure S4d). Based on this result, 0.1 K^2 (100 km)$^{-2}$ hr^{-1} is chosen as the threshold for FF.

In summary, among the waves of which ray is terminated in the layer of 0–6 km (Figure 3), if any of the FF calculated at pressure levels within 2 km from the ray termination altitude using 6-hourly ERA-Interim data gridded at 0.75° × 0.75° (lat. × lon.) is greater than a threshold value of 0.1 K^2 (100 km)$^{-2}$ hr^{-1} in the diagnostic area within 3 hr (Table 1, ii), a front is suggested as a potential source. Note that the presence of a front has not been considered poleward of 75°S because of the high sensitivity to anomalies in the data assimilation process at these latitudes, which can render the analysis data not trustworthy (Charron & Manzini, 2002). In addition, anomalous small-scale frontal regions along the coastal lines of the Antarctic continent affected by the strong temperature gradient are not considered to be coherent frontal activities (Figure S4). Therefore, the region with a topographic slope greater than 15 m km^{-1} is excluded from the frontal region.

3.2.2. A Case of a Front Source

Figure 5 describes a case of wave generation accompanying frontogenesis. The corresponding IGW was observed at JBS on 15 February 2017. The ray was traced down to 0.16-km altitude at the horizontal location of 46.51°S and 136.23°E. The total integration time of 95.05 hr indicates that the wave originated at approximately 00 UTC on 11 February 2017 (Figure 5a). Figure 5b illustrates the potential temperature and FF calculated at 850 hPa at the time of probable GW generation in the fan-shaped area in Figure 5a. Significant latitudinal variations in the potential temperature (from 286 K to 306 K) and coincident strong frontogenesis appear with an FF approaching 3 K^2 (100 km)$^{-2}$ hr^{-1} between 40°S and 48°S. This wave is unlikely to be the orographic origin because the termination position is far from the significant terrain. Furthermore, there was no pronounced convective activity (not shown). Thus, the only possible source of the IGW event in the troposphere is the frontal activity.

To examine the existence of waves forced by frontal activities, the vertical wind perturbation and potential temperature at 800 hPa (above the frontogenesis level of 850 hPa) at 00 UTC on 11 February 2017 are plotted
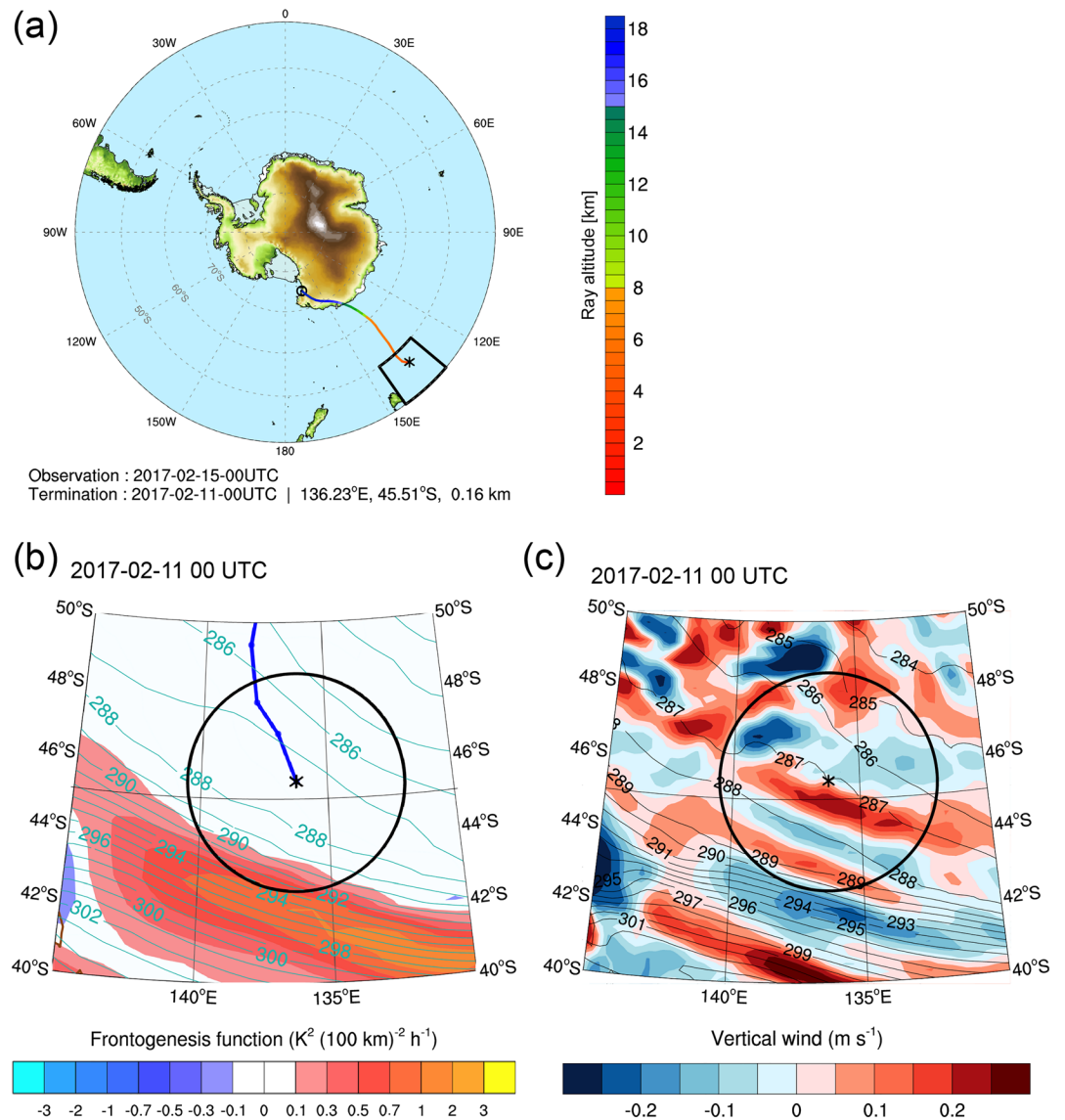
Figure 5. (a) Ray back trajectory of the IGW observed on 15 February 2017. The start and termination positions of the ray are marked with black double circles and asterisks, respectively. (b) Zoomed map of the black fan-shaped area in (a). The ray back trajectory (blue line) of the IGW is superimposed on the FF (shading) and potential temperature (cyan line) at 800 hPa at 00 UTC on 11 February 2017. The black circle represents the diagnostic area. (c) Vertical velocity perturbation (shading) at 650 hPa with potential temperature (black line) at 800 hPa at 00 UTC on 11 February 2017.

in Figure 5c. Pronounced oscillations occur above the active frontogenesis region, accompanying the significant gradient of isothermal lines. Although convection is not detected based on the criterion for selecting convection of the current study (hourly precipitation inside the diagnostic area is larger than 2.5 mm hr^{-1}), weak convective activities are identified from the infrared (IR) brightness temperature of 250–255 K inside the diagnostic area (not shown). This suggests that the frontal GWs shown in Figure 5c could be enhanced due to the moist process, which has been reported by Wei and Zhang (2014). Those waves have phase lines parallel to the along-front direction and strong amplitudes of vertical wind fluctuations of approximately 0.3 m s^{-1}. This feature is quite similar to the result of the idealized baroclinic instability simulations of Kim et al. (2016), where the frontal GWs generated by the low-level baroclinic waves have phase lines parallel to the isentropic lines (see Figure 2 therein). Thus, GW events identified in ERA5 seem to be triggered by the frontal activities. The horizontal wavelength deduced from

the vertical wind perturbations is approximately 170–190 km, which is somewhat longer than those of 80–150 km obtained from GROGRAT (Figure S6b). The phase lines aligned parallel to the cross-front lines in the vertical wind perturbations are consistent with the dominant southwestward wave vectors estimated from GROGRAT (Figure S6b).

3.3. Identification of the Convection Source
3.3.1. Diagnostic Method

Extremely cold and dry atmosphere around JBS inhibit the development of convection near the station. However, the possibility of convection as a source for the observed IGWs cannot be completely ruled out because the observed IGWs can propagate long horizontal distances from their source regions. Ern et al. (2011) showed that GWs generated by deep convections in the tropics and subtropics can travel to the midlatitudes and even polar regions according to satellite observations.

To identify GWs associated with convection sources, we first estimate the occurrence of convection at the termination locations. Chun et al. (2007), Ki and Chun (2010), and Ki and Chun (2011) adopted the deep convective activity obtained using the brightness temperature in the infrared band as a proxy for the convection in the subtropical region. Similarly, Pramitha et al. (2015, 2016) used satellite data of outgoing long-wave radiation to obtain information on synoptic-scale convection in the tropics. However, there are apparent latitudinal variations in the cloud top height estimated by outgoing longwave radiation and the IR brightness temperature, which decrease from the tropics to the polar regions. This makes it difficult to apply the abovementioned diagnostics in this study to determine the existence of convective clouds in the middle to higher latitudes. One alternative indicator for the presence of convection is precipitation. Chun et al. (2006, 2007) also investigated the characteristics of GWs associated with convective activity using hourly accumulated precipitation data. However, it is true that convection does not necessarily accompany precipitation and the convective cells producing precipitation are highly intermittent and localized (Chun et al., 2006). Nevertheless, given that precipitation rates are closely related to the depth and strength of moist convection, which is an important generation mechanism of GWs (Holt et al., 2017), precipitation rates are thought of as providing valuable information on the occurrence of convection without significant latitudinal dependence. Therefore, in the present study, precipitation is used as a proxy to estimate the presence of convection using the hourly precipitation data sourced from the Level 3 Integrated Multi-satellitE Retrievals for Global Precipitation Measurement precipitation Version 5 (V05) product at 0.1° latitude and longitude (Huffman et al., 2017). The use of hourly accumulated precipitation data with a high spatial resolution allows for analyzing the localized and short-lived convective precipitation events with high rainfall intensities.

There is no specific threshold of precipitation rate indicating the presence of convection. Therefore, we assume that moderate precipitation and heavy precipitation are associated with convective clouds. While heavy precipitation is mostly triggered by deep convective clouds, moderate precipitation is likely caused by stratiform clouds as well as shallow convection. Nevertheless, the minimum precipitation defining convective activity is employed as the threshold of moderate rainfall intensity to include the dominant shallow convective clouds in the higher southern latitudes. According to the classification of convective rainfall intensity by the United Kingdom Meteorological Office (UKMO, 2007), the threshold value of the rain rate representing the occurrence of convective clouds is set to 2.5 mm hr^{-1}. Therefore, among the waves of which ray terminated in the layer of 0–8 km (Figure 3), if any of the hourly Integrated Multi-satellitE Retrievals for Global Precipitation Measurement precipitation within 3 hr from the time of wave generation is greater than a threshold value of 2.5 mm hr^{-1} inside the diagnostic area, convection is regarded as a possible source (Table 1, iii).

3.3.2. A Case of the Convective Source

A case of the convective IGWs is examined in Figure 6. The corresponding wave was observed at JBS on 31 October 2017. As shown in the ray trajectory in Figure 6a, the wave is traced down to 3.14-km altitude at the horizontal location of 50.33°S and 95.35°E. Given that the ray propagated for 49.18 hr, we can deduce that wave generation occurred at approximately 22 UTC on 28 October 2017. The presence of convection is examined in Figure 6b, which shows the hourly accumulated precipitation amount at 22 UTC on 28 October 2017 in the fan-shaped area of Figure 6a. At the time of wave generation, an intense rainfall area appears with the maximum precipitation amount approaching 10 mm hr^{-1} centered on the wave generation location. This
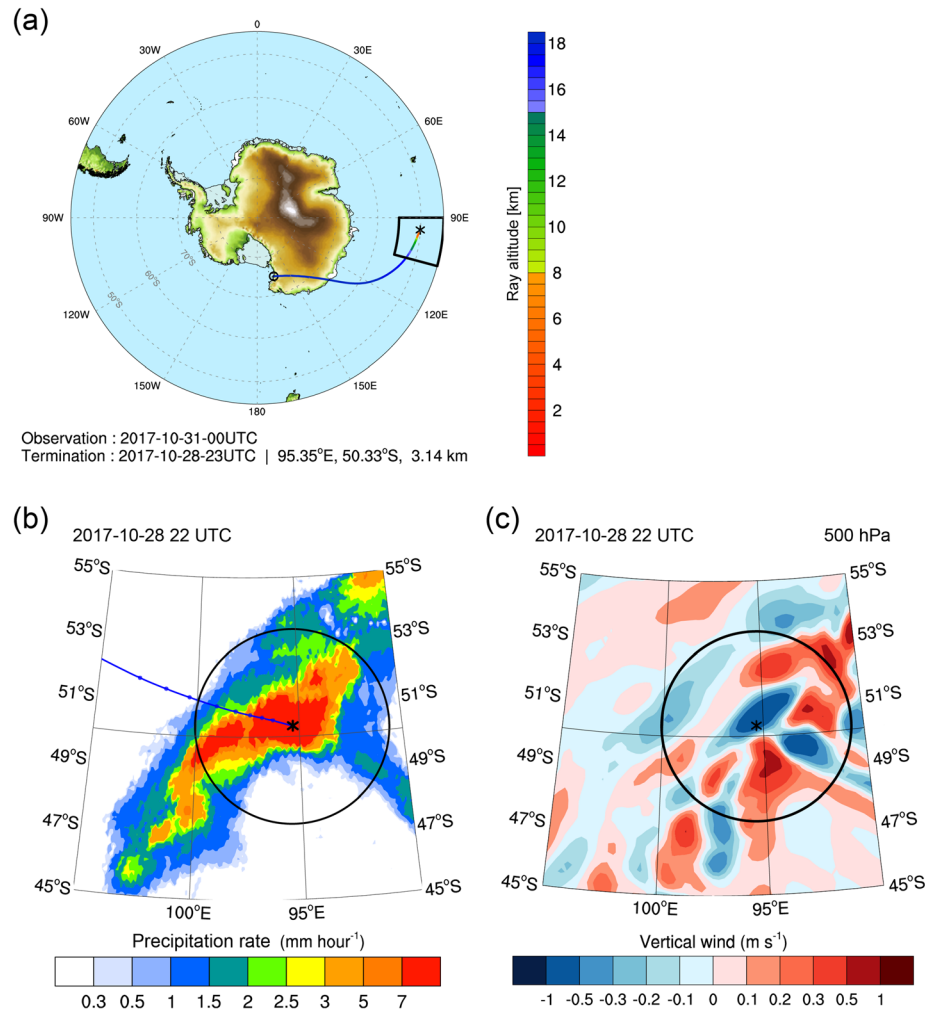
Figure 6. (a) Ray back trajectory of the IGW observed on 31 October 2017. The start and termination positions of the ray are marked with black double circles and asterisks, respectively. (b) Zoomed map of the black fan-shaped area in (a). The ray back trajectory (blue line) of the IGW is superimposed on the IMERG hourly precipitation at 22 UTC on 28 October 2017. The black circle represents the diagnostic area. (c) Vertical velocity perturbation at 500 hPa at 22 UTC on 28 October 2017.

heavy precipitation greater than the threshold indicates that the convective cloud exists within and around the diagnostic area. As shown in Figure 6a, the termination position lies over the Southern Ocean far away from the mountainous regions. Furthermore, no pronounced frontal activity was detected in the region based on the analysis of FF. Thus, the most plausible source for the observed IGW is convective clouds accompanying the strong precipitation.

We analyze the vertical wind perturbation obtained from ERA5 to examine the GW associated with the convective activity in Figure 6c. Investigation of the vertical wind perturbation is carried out at 500 hPa (approximately 4.5 km), which is somewhat above the altitude of wave emission, at 22 UTC on 28 October 2017. Within the diagnostic area, complex wave signatures with large amplitudes are identified due to the overlap of the two prominent waves: the wave packet having phase lines in the southwest-northeast direction in the eastern side of the diagnostic area, and the other wave packet having phase lines aligned in the southeast-northwest direction in the western side of the diagnostic area. Considering that the horizontal wavenumber vectors estimated from GROGRAT direct eastward dominantly, the first wave packet seems to have similar characteristics to those from GROGRAT. The horizontal wavelengths of the wave obtained from GROGRAT (55–85 km) are, however, shorter than that estimated from ERA5 (180 km) (Figure S6c).

3.4. Flow Imbalance Source Associated With the Jet Stream

3.4.1. Diagnostic Method

The upper-tropospheric jet/front system has long been recognized as a major source of GWs. Numerous observational (e.g., Fritts & Nastrom, 1992; Guest et al., 2000; Plougonven & Teitelbaum, 2003) and modeling studies (e.g., Plougonven & Snyder, 2007; Sato et al., 2012; Wang & Zhang, 2007; Zhang, 2004) have investigated the configuration of specific flow and possible mechanisms for the emission of GWs associated with the jet/front system. Typically, these waves have low intrinsic frequency, short vertical wavelengths, and relatively longer horizontal wavelengths and appear predominantly in the jet exit region and often upstream of a ridge in the geopotential field. Regarding the mechanisms responsible for GW emission by the upper level jet/front system, classical geostrophic adjustment, Lighthill radiation, unbalanced instabilities, transient generation, and shear instability have been proposed (Plougonven & Zhang, 2014). We mainly investigate the GW generation induced by the flow imbalance in the present study.

Various diagnostics of the flow imbalance have been used to diagnose the emission of GWs, including the Lagrangian Rossby number, which represents the departure from the geostrophic balance (e.g., O'Sullivan & Dunkerton, 1995; Spiga et al., 2008). As a more sophisticated indicator of the flow imbalance, Zhang et al. (2000) introduced the residual of the nonlinear balanced equation (hereafter RNBE), which has been widely used in many studies (e.g., Chun et al., 2019; Ki & Chun, 2011; Kim et al., 2011; Limpasuvan et al., 2011; Murphy et al., 2014; Part 1; Sato & Yoshiki, 2008; Sharman et al., 2006; Song et al., 2017). In the present study, the flow imbalance is evaluated using the global formulation of RNBE (Chun et al., 2019) as in Part 1 with 6-hourly ERA-Interim data gridded at 0.75°. In order to exclude the contribution of grid-resolved GWs in RNBE (Zhang, 2004), a low-pass filter with cutoff zonal Wavenumber 22 is applied to the reanalysis data in the calculation of RNBE, as in Part 1.

To determine the diagnostic altitude and threshold value for RNBE, we investigated the occurrence rate of the RNBE magnitude (hereafter |RNBE|) for each pressure level in the tropopause and stratospheric analysis layer (450–70 hPa) in each season compiled at all longitudes in the three latitudinal bands (45–55°S, 55–65°S, and 65–75°S) (Figure S5). Within the analysis layer, the distribution of |RNBE| does not have obvious latitudinal or height dependency, except for the tropopause layer (450–300 hPa), in which the values have a wider distribution with higher values. This implies that the imbalance could occur anywhere throughout the analysis layer. Hence, the diagnostic level for identifying the flow imbalance is not determined as a single level, but every pressure level within 2 km of the termination altitude. Meanwhile, the values of |RNBE| are dominantly less than 1×10^{-9} s^{-2}, with a pronounced maximum frequency at approximately 0.4×10^{-9} s^{-2}. However, |RNBE| itself represents the degree of imbalance, not the occurrence of GW generation by the flow imbalance. Therefore, we need to select a certain threshold value for |RNBE|, indicating the excitation of GW associated with the imbalance. Based on the occurrence rate in Figure S5, the threshold value is set to 1.5×10^{-9} s^{-2} corresponding to the upper 10% of the distribution that is considered to be imbalance strong enough to produce GWs. In summary, among the waves of which ray terminated in the layer of 8–18.5 km (Figure 3), if any of the |RNBE| calculated at the pressure levels within 2 km from the ray termination altitude exceeds a threshold value of 1.5×10^{-9} s^{-2} in the diagnostic area within 3 hr, the flow imbalance is suggested as a possible source (Table 1, iv). In addition, in the tropopause region, if the wind velocity is greater than 20 m s^{-1} (Table 1, v), we further specify that the flow imbalance exciting GWs is associated with the upper-tropospheric jet stream. As with the same aforementioned reasons in FF (section 3.2.1), the presence of flow imbalance is not considered poleward of 75°S (Chun et al., 2019).

3.4.2. A Case of the Flow Imbalance Source Induced by the Jet Stream in the Tropopause

Figure 7 presents a case of GWs induced by the flow imbalance. This IGW was detected at JBS on 26 March 2016. The ray back trajectory in Figure 7a shows that the wave is traced down to an altitude of 13.17 km at 55.53°S and 16.14°E, which is horizontally far from the station. Given that the ray propagated for approximately 5 days, the generation is likely to occur at 00 UTC on 21 March 2016. As the termination position is located in the tropopause layer, we investigate |RNBE| and zonal wind distribution at 175 hPa (approximately 12.6 km) in Figure 7b to examine the possibility of wave generation by the flow imbalance. A significantly imbalanced flow with a pronounced maximum in |RNBE| of greater than 3×10^{-9} s^{-2} is identified across a wide area of 57–63°S and 5–20°E. Given that the imbalanced flow is located in the exit region of the jet streak having the maximum wind speed of 45 m s^{-1}, we can infer that this imbalance flow is
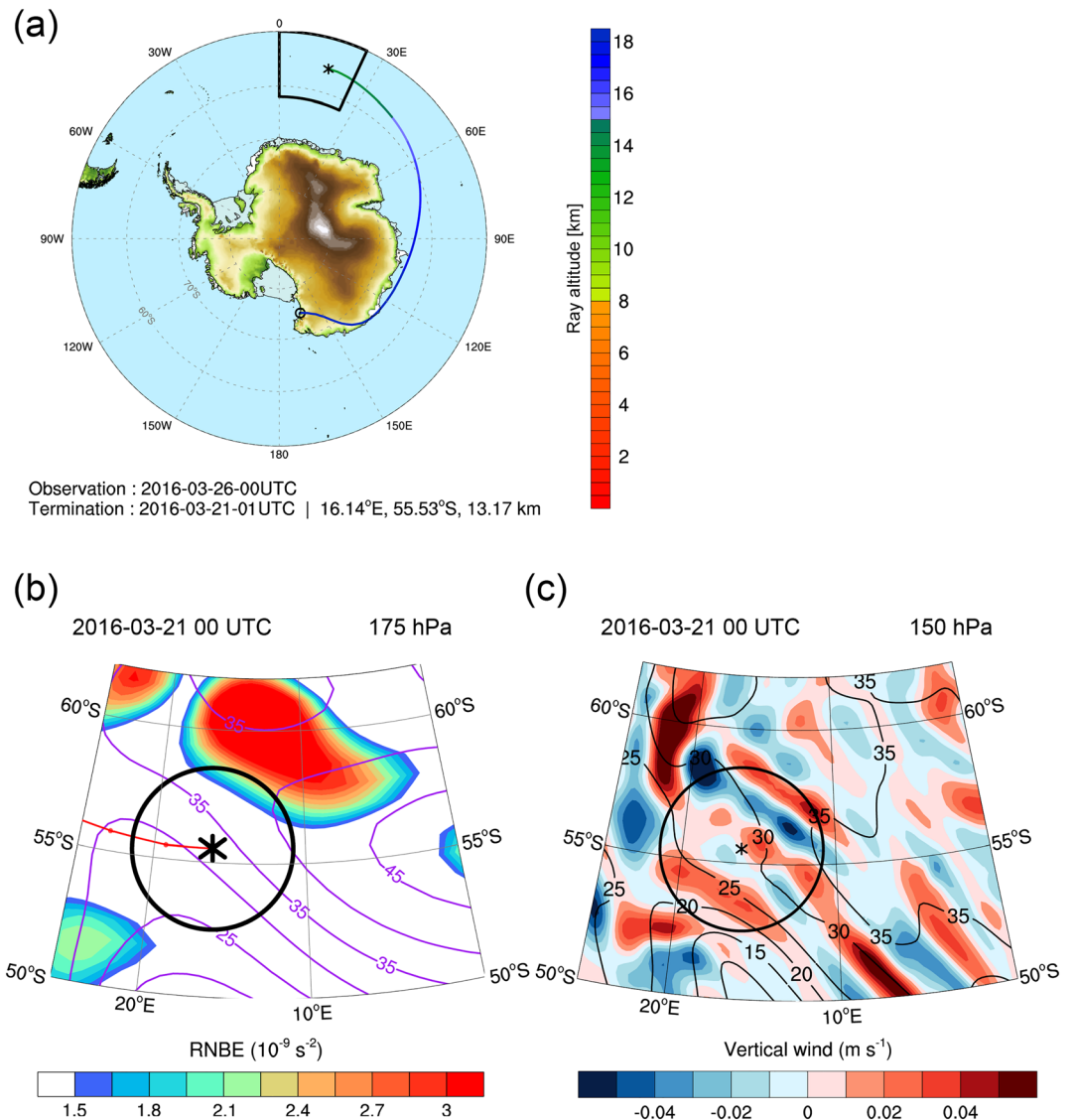
Figure 7. (a) Ray back trajectory of the IGW (red line) observed on 26 March 2016. The starting and termination positions of the ray are marked with black double circles and asterisks, respectively. (b) Zoomed map of the black fan-shaped area in (a). The ray back trajectory (red line) of the IGW is superimposed on the |RNBE| (shading) and horizontal wind speed at 175 hPa at 00 UTC on 21 March 2016. The black circle represents the diagnostic area. (c) Vertical velocity perturbation (shading) with the horizontal wind speed (black line) at 150 hPa at 00 UTC on 21 March 2016.

associated with the jet stream. Therefore, the observed IGW is thought to be associated with the significantly imbalanced flow at the jet exit region, which has been identified as a favorable location of GW generation (Uccellini & Koch, 1987).

Using the vertical wind perturbations obtained from ERA5, we investigate whether the GWs induced by the imbalanced flow appear. Figure 7c shows the vertical wind perturbation with the zonal wind speed at 150 hPa (approximately 13.6-km altitude; just above the altitude of possible wave generation). Within and around the diagnostic area, the vertical wind perturbations exhibit distinct but complex patterns of alternating positive and negative signs with a maximum magnitude of approximately 0.05 m s^{-1} directly downstream of the imbalanced flow. Furthermore, the wave has phase lines that are mostly parallel to the lines of constant wind speed, which is similar to the waves spontaneously emitted by the localized jet in the exit region in Wang et al. (2009). This result suggests that the generation of the identified GW is associated with
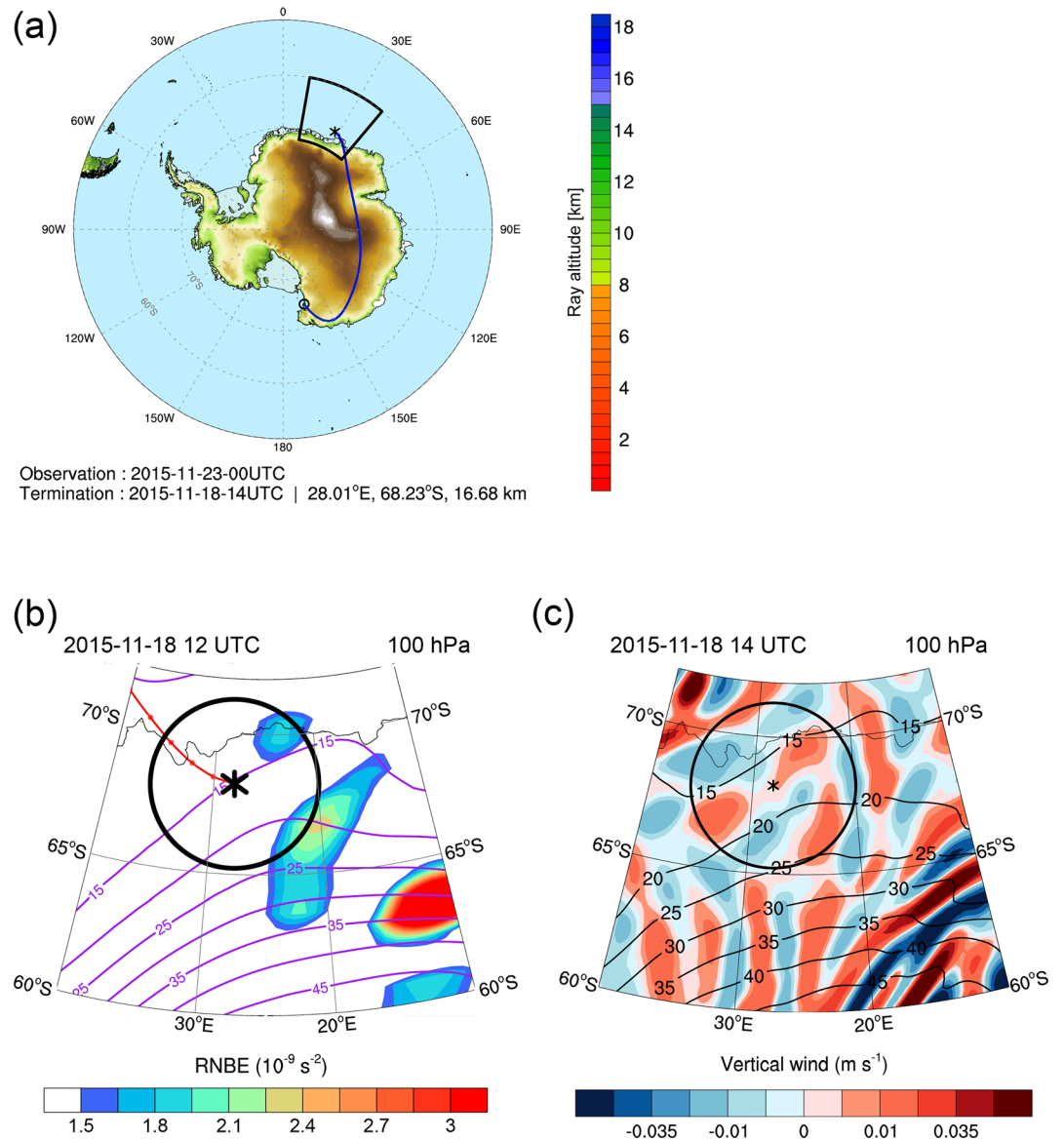
Figure 8. (a) Ray back trajectory of the IGW observed on 23 November 2015. The start and termination positions of the ray are marked with black double circles and asterisks, respectively. (b) Zoomed map of the black fan-shaped area in (a). The ray back trajectory (red line) of the IGW is superimposed on the |RNBE| (shading) and horizontal wind speed at 100 hPa at 12 UTC on 18 November 2015. The black circle represents the diagnostic area. (c) Vertical velocity perturbation (shading) with the horizontal wind speed (black line) at 100 hPa at 14 UTC on 18 November 2015.

the flow imbalance appearing in the immediate exit region of the jet core. The horizontal wavelength of GWs derived from the vertical perturbation is approximately 206 km, which is somewhat shorter than those of 270–400 km obtained from GROGRAT (Figure S6d). The wave vectors from GROGRAT mostly direct east and southeastwards (Figure S6d), which is somewhat different from the northeastward vector of the predominantly identified GW in ERA5.

3.4.3. A Case of the Flow Imbalance Source in the Stratosphere

The GW generation by the flow imbalance in the stratosphere is examined in Figure 8. The diagnostic method is the same as that described in section 3.4.2. This wave is detected in the radiosonde sounding launched at 00 UTC on 23 November 2015. As seen in the backward ray trajectory illustrated in Figure 8a, the ray mostly propagates horizontally for 105 hr from JBS to the location of 68.23°S and 28.01° E at a 16.68-km altitude. According to the propagation time, we can infer that GW generation occurred

Table 2
The Number of Rays Categorized in Each Potential Source

Termination layer	Potential source	The number of GWs	Uncategorized
Stratosphere (68)	Flow imbalance	42	26
Tropopause (68)	Flow imbalance/Jet stream	36/11	32
Troposphere (112)	Orography	35	35
	Surface front	37	
	Convection	28	

near 14 UTC on 18 November 2015. Figure 8b represents the horizontal wind speeds superimposed on |RNBE| at 100 hPa (approximately 16.1-km altitude) at 12 UTC on 18 November 2015. On the northeast side of the diagnostic area marked by the black circle in Figure 8b, significant horizontal wind shear from the region of maximum wind speed attaining 45 m s^{-1} and |RNBE| approaching 2.4×10^{-9} s^{-2} is identified, implying that the flow is considerably unbalanced in that region.

Figure 8c shows the vertical wind perturbation with the horizontal wind speed at 14 UTC on 18 November 2015 at 100 hPa. The most significant fluctuations exceeding 0.05 m s^{-1} are shown in the maximum wind speed region (60–65°S and 10–20°E). Relatively weak fluctuations extending from the strongest fluctuations appear predominantly in the northwest side of the diagnostic area, which corresponds to the |RNBE| exceeding the threshold value in Figure 8b. This structure suggests that the GW signals inside the diagnostic area are obviously associated with the imbalanced flow. However, we cannot entirely rule out the possibility that those GW signatures may originate and propagate from the higher RNBE regions located at 60–65°S and 10–20°E. The horizontal wavelength of GWs inferred from the vertical wind perturbation is approximately 200–300 km, which is somewhat longer than those of 100–145 km obtained from GROGRAT (Figure S6e). The wave vectors derived from GROGRAT direct southwestwards (Figure S6e), which is also different from the dominant southeastward wave vector of GWs in ERA5.

4. GWs With Respect to the Potential Sources

Based on the methods for identifying the potential sources of GWs introduced in section 3, we categorized the observed IGWs into the probable sources and examine their statistical characteristics. Table 2 lists the number of IGW cases classified into the potential sources. Note that multiple sources can be simultaneously suggested for each wave event. Out of 112 waves that originate in the troposphere, 37 (33%), 35 (31%), and 28 (25%) IGW events are categorized into the frontal activity, orography, and convection, respectively. For 11 (9%) cases, both a front and convection are simultaneously selected as potential sources, whereas 5 (4%) and 6 (5%) cases are classified into both orographic and frontal GWs and both orographic and convective GWs, respectively. Among the 68 waves generated in the stratosphere, 42 (61%) waves are related to the flow imbalance, while in the tropopause a relatively small portion (52%; 36/68) of the waves are associated with the flow imbalance. Of the 36 waves induced by the imbalanced flow in the tropopause region, 11 waves (30%) are associated with the tropopause jet stream.

Unfortunately, a large number of waves generated in the troposphere (35/68; 31%) cannot be classified as any of the proposed tropospheric origins. Similarly, for a large portion of the waves produced in the tropopause (47%; 32/68) and in the stratosphere (38%; 26/68), the likely source is not specified. Most of the rays of these waves are terminated poleward of 75°S (not shown) on the Antarctic Plateau, which is characterized by a flat surface that could hardly generate orographic GWs. Also, convection and fronts are rarely developed in this high latitude region due to the extremely cold and stable atmosphere. This implies that other potential GW sources that we did not consider in this study may exist in this region. It is noteworthy that the number of IGW cases varies depending on the threshold values used for the identification method. When we changed the threshold values in the range of ±10% from their original values for each source (not shown), the number of frontal GWs is nearly the same, whereas the numbers of GWs associated with other sources (orography, convection, and the flow imbalance) vary within 15%.

4.1. Geographic Distributions of Wave Generation

Figure 9 illustrates the ray trajectories of each wave assorted by the potential sources. To investigate the seasonal characteristics of the propagation and source regions, the ray trajectories are plotted in different colors with respect to the season when each wave is observed.

Depending on the sources, the locations of wave generation and the raypaths to JBS are clearly distinguished. Orographic GWs mostly originate above the significant orographic slopes located west of the Ross Sea (Figure 9a), whereas convective GWs are mainly generated above the ocean (Figure 9c). Approximately 30% (8 out of 28 waves) of the convective GWs propagate from the low latitudes equatorward of 60°S, which is consistent with the significant lateral propagation of convectively induced GWs toward southern polar regions from SH storm track regions, as reported in Choi and Chun (2013). The frontal GWs are generated across wide regions from the midlatitude Southern Ocean to mainland Antarctica (Figure 9b). The Southern Indian Ocean, over which a lot of convective and frontal GWs are generated, is consistent to the active region of nonorographic GWs (Hendricks et al., 2014). While most of the waves induced by the tropospheric sources propagate from the eastern hemisphere (0–180°), many of the waves associated with the imbalanced flow in the tropopause and stratosphere are generated along all longitudes in the higher southern latitudes poleward of 50°S (Figures 9d and 9e). Accordingly, those waves predominantly travel horizontally rather than vertically from their source regions to JBS, spending a relatively long time compared to the time spent by the waves of tropospheric origins. Although details in the propagation properties vary depending on their sources, significant horizontal propagations of the GWs, especially those of nonorographic origins, indicate that GWD parameterization based on ray theory is required in GCMs for better representation of GWs (Choi & Chun, 2013; Senf & Achatz, 2011; Song & Chun, 2008).

4.2. Seasonal Variations in the Occurrence of GWs

As shown in Figure 9, remarkable seasonal variations appear not only in the occurrence frequency with respect to each source but also in the generation locations and corresponding propagations of GWs. Table 3 lists the occurrence frequency of GWs with respect to each source in each season. Note that the number of observed IGWs used for the ray tracing analysis during wintertime (20) is considerably less than that in other seasons (87, 77, and 65 waves in summer, autumn, and spring, respectively) due to the small number of the observed IGWs during wintertime (mentioned in section 2). Therefore, some caution is required to analyze the seasonal variations in the GW generation for this study.

Most of the orographic GWs (65%; 23/35) are generated in summer, whereas only one orographic GW (2%) is found to be excited in winter. Similarly, convective GWs are dominantly excited during summer (60%; 17/28), while in winter, convectively induced GWs are not identified. In comparison to the orographic and convective GWs, the frontal GWs have comparable occurrence frequencies in all seasons without obvious differences, except for the small number of GWs during wintertime. In the tropopause, GWs associated with the flow imbalance do not exhibit pronounced seasonal variations. On the other hand, interestingly, the occurrence frequency of GWs generated by the imbalanced flow associated with the jet stream reveals obvious seasonal variations with significantly lower probability (8%; 1/12) during summer in comparison to those (28%, 50%, and 62% in autumn, winter, and spring, respectively) in other seasons, although the total case during winter is already small. In the stratosphere, GWs induced by the flow imbalance appear most frequently in spring (40%; 17/42). It is also noticeable that 55% (11/20) of the waves observed in winter are generated in the stratosphere, and most of them (81%; 9/11) are associated with the flow imbalance.

There are two major factors that result in the seasonal variations in the occurrence frequency of GWs: (i) variations in the GW source itself and (ii) wave propagation conditions from the source to the observation altitude (i.e., impact of background wind and stability) (Kang et al., 2017). For a stationary mountain source, seasonal variation of orographic GWs is due mainly to (ii) depending on the transient background atmosphere around the mountain. As an example, Watanabe et al. (2006) have shown that the orographic GW generation and its vertical propagation mostly occur during winter and spring in the western coastal region of the Ross Sea due to an enhanced katabatic wind when the upper-tropospheric jet stream approaches the Ross Sea. While the locations of the orographic GW excitations identified in Figure 9a is similar to that in
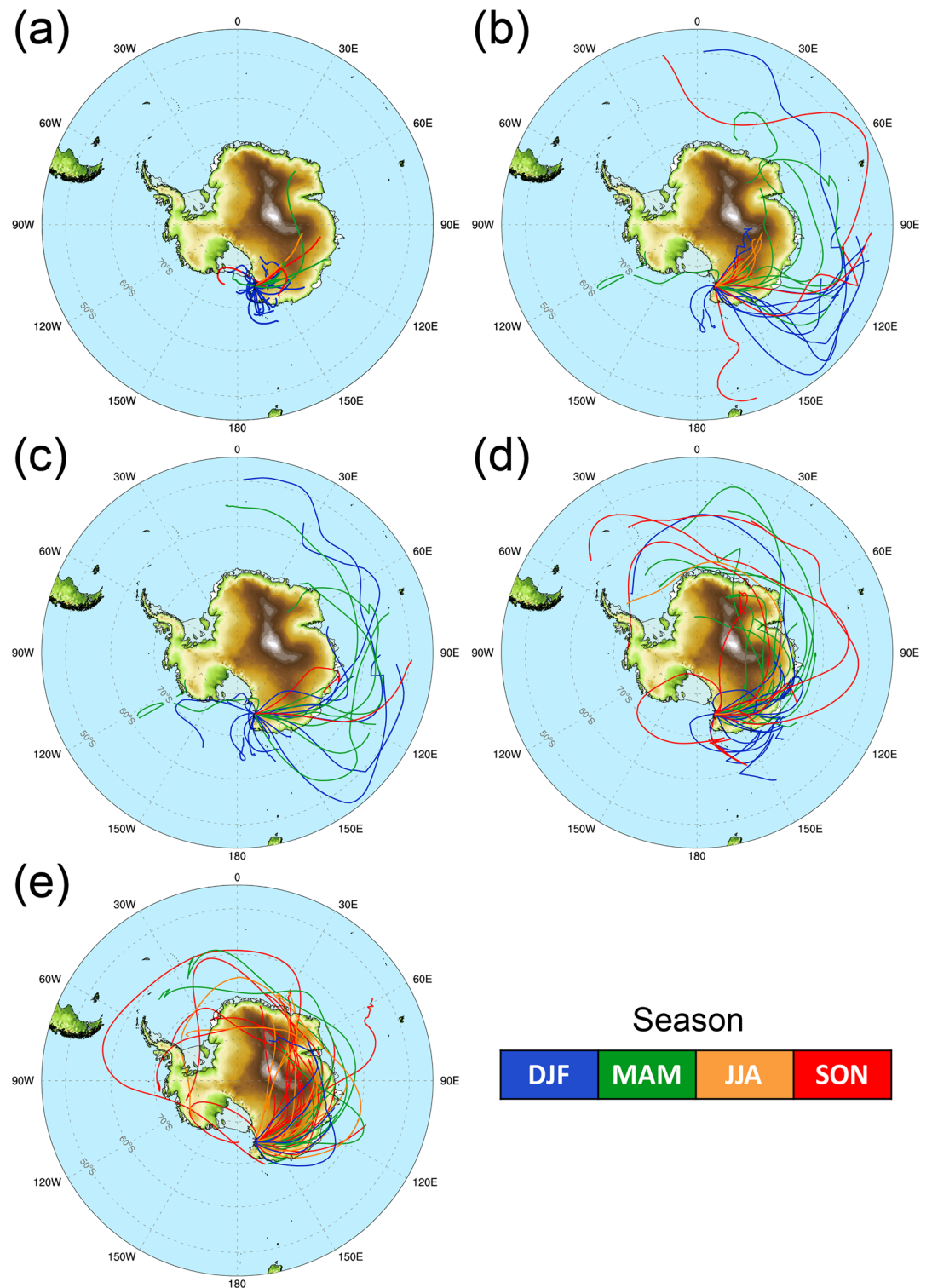
Figure 9. Back trajectories of the rays associated with the (a) orography, (b) front, (c) convection, (d) the flow imbalance in the tropopause, and (e) the flow imbalance in the stratosphere. The colors of each ray trajectory represent the season in which the wave is observed.

Table 3
The Number of Rays Categorized in Each Potential Source in Each Season

Termination layer	Potential source	Summer (DJF)	Autumn (MAM)	Winter (JJA)	Spring (SON)
Troposphere	Orography	23	6	1	5
	Surface front	13	12	4	8
	Convection	17	8	0	3
	Total including uncategorized	49	29	5	29
Tropopause	Flow imbalance/ jet stream	12/1	14/4	2/1	8/5
	Total including uncategorized	23	28	4	13
Stratosphere	Flow imbalance	6	10	9	17
	Total including uncategorized	15	20	11	23

Watanabe et al. (2006), the observed mountain waves are mostly generated in summer, which is somewhat unexpected. The small number of observations during the wintertime can reduce the opportunity for detecting the orographic GWs. There are some other potential explanations for the seasonal variations. First, critical levels for the orographic waves may exist, inhibiting their propagation to the lower stratosphere. Hertzog et al. (2008) reported that the lack of GW enhancement at the border of Antarctica is possibly due to the critical level filtering of orographic GWs by the veering wind from the dominant south or south-southeastward katabatic wind to the prevailing eastward stratospheric flow (at least 90°). However, it is not enough to explain the seasonality given that this kind of filtering can also take place during other seasons. More feasible reason for the lack of observed orographic GW during wintertime is likely the Doppler shifting of GWs out of the observational window. The vertical wavelength for the hydrostatic GW dispersion relation is as follows:

$$\lambda_z = \frac{2\pi(C - U\cos \phi)}{N} \tag{5}$$

where N is the background buoyancy frequency, C is the ground-based horizontal phase speed, U is the background wind speed, and ϕ is the angle between the horizontal wavenumber vector and the wind vector. Given that the orographic GWs have near-zero phase speed, strong background winds during austral wintertime can significantly refract the orographic GWs to long vertical wavelengths as well as enhance their vertical propagation. Considering that the radiosonde can mainly detect low-frequency GWs, the orographic GWs refracted to a long vertical wavelength and a higher intrinsic frequency cannot be observed from the radiosonde. Additionally, the mountain waves, which are generated horizontally far away from the station, can hardly reach JBS due to the enhancement in the vertical propagation rather than horizontal propagation. Therefore, those waves also cannot be detected from the radiosonde observations in wintertime launched from JBS. Finally, the dominant eastward drift of the balloons away from the steep coasts of the Antarctic continent during winter and early spring (Figure 2 of Part 1) can also reduce the likelihood of observing orographic GWs.

As shown in Figure 9c, convective GWs are mostly excited above the Antarctic polar frontal zone. In this region, precipitation, which is used for diagnosing the presence of convection in this study, varies significantly with season: It increases (decreases) from January to April (from May to December) (Yuan & Miller, 2002). Hence, we can infer that the more frequent occurrence of precipitation in summer is reflected in the dominant generation of convective GWs during the summertime. Similarly, the excitation of the frontal GWs occurs frequently above the Southern Indian Ocean during summertime (Figure 9b). All six waves, for which convection and fronts are simultaneously suggested as potential sources, are excited above the Southern Ocean during summer and autumn (not shown). This implies that there is a close link between the frontal system and convection on the SH storm track regions and they simultaneously trigger GWs. This behavior has also been recognized from the high-resolution GCM simulation in Holt et al. (2017)
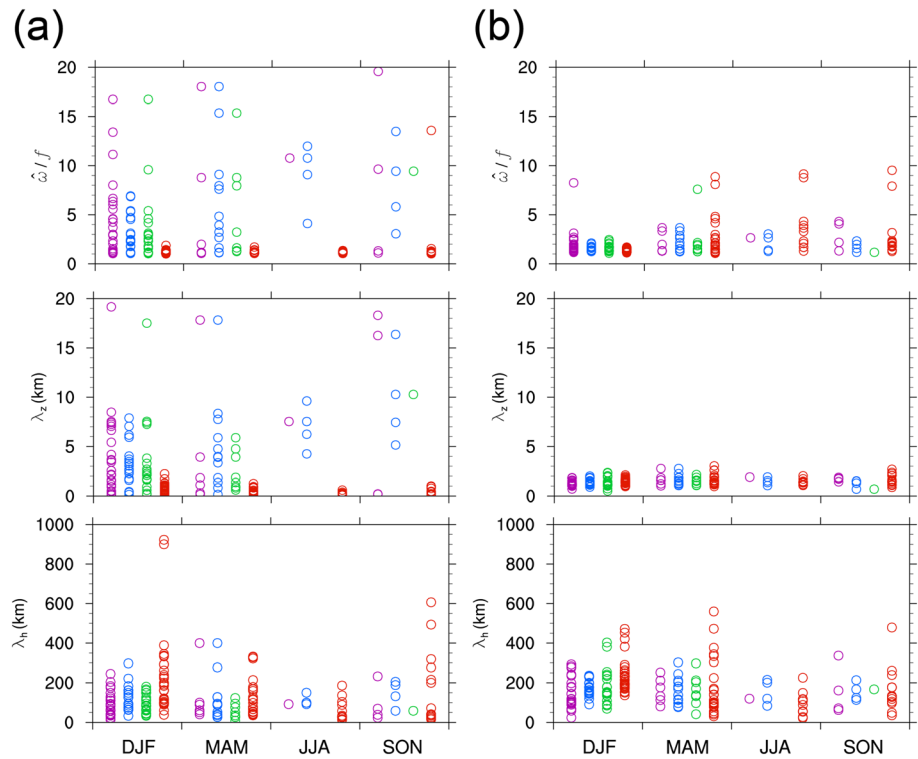
Figure 10. Intrinsic frequency divided by Coriolis parameter (first row), vertical wavelength (second row), and horizontal wavelength (third row) for each wave associated with orography (purple circle), front (blue circle), convection (green circle), and flow imbalance (red circle) at the time of (a) generation and (b) observation.

that gravity wave momentum flux induced by the fronts and precipitation are closely correlated at latitudes of 30–80°S, although the study focuses on the wintertime.

Comparable occurrence frequencies of GWs associated with the flow imbalance in the tropopause in all seasons (Table 3) reflect the continuous generation of the flow imbalance representing large RNBEs for all seasons in the tropopause region (Figure S5). This is different from the GWs associated with the jet stream, which exhibit obvious seasonal variations with the highest (lowest) probability in spring (summer) as the position of the southern polar front jet moves to middle and higher southern latitudes from late autumn to spring (Gallego et al., 2005). This implies that there are other mechanisms triggering the flow imbalance near the tropopause, in addition to the tropopause jet stream. The synoptic-scale tropospheric disturbances, which are responsible for the enhanced stratospheric GW activity above Antarctica reported by Hertzog et al. (2008) and Yoshiki et al. (2004), can be a candidate. Additionally, the terrain-induced baroclinic wave development identified in Hoskins and Hodges (2005) also can be a source for the flow imbalance. In the stratospheric analysis layer, RNBE greater than the threshold value appears more frequently in winter (JJA) and spring (SON) than autumn (MAM) and summer (DJF) (Figure S5) as the horizontal wind speed as well as their horizontal shear increases. This variability results in seasonality in the occurrence frequency of GWs associated with the flow imbalance in the stratosphere, which is higher in winter and spring than in summer.

4.3. Spectral Properties of GW With Respect to the Source
4.3.1. Intrinsic Frequency and Wavelengths
Figure 10 shows the scatterplots of intrinsic frequency, vertical wavelength, and horizontal wavelengths of GWs with respect to the potential sources in each season when those waves are generated (left column) and observed from the radiosonde (right column). GWs induced by the tropospheric sources (orography, fronts, and convection are represented by purple, blue, and green circles, respectively) have a wide range

of intrinsic frequencies and vertical wavelengths of 1–20f and 0.5–10 km, respectively. On the other hand, the waves induced by the flow imbalance (red circles) exhibit pronounced low intrinsic frequencies and short vertical wavelengths of less than 2f and 3 km, respectively. Based on the dispersion relation, the horizontal wavelengths of the tropospheric GWs have narrower range ($\leq$ 200 km) than the range ($\leq$ 400 km) of the GWs associated with the flow imbalance. Characteristics of GWs related to the flow imbalance agree remarkably well with the dominant properties (low intrinsic frequency of ~1–3f, short vertical wavelength of ~1–4 km, and long horizontal wavelength 50–500 km) of GWs associated with the upper-level jet/front system in previous numerical modeling studies (e.g., Plougonven & Snyder, 2007; Zhang, 2004) and observational studies (e.g., Guest et al., 2000; Plougonven & Teitelbaum, 2003). In contrast, the intrinsic frequency and wavelengths of GWs generated by the tropospheric sources are not largely different from each other.

As shown in the characteristics of GWs at the time when they are observed from the radiosonde (Figure 10b), the widely distributed properties of the tropospheric GWs at the source level as well as those of GWs associated with flow imbalance converge to similar characteristics: a low frequency of mostly less than 4f and a shorter vertical wavelength of less than 3 km. The vertical wavelength of GWs detected from the radiosonde data is generally influenced by the observational filtering effect (Alexander, 1998), including a depth of the stratospheric analysis layer (7 km in the present study). However, the prevalent vertical wavelengths of less than 3 km are identified in both an additional calculation under deeper stratospheric layer calculation using the present data and some of previous studies in the Antarctica with much deeper layers (details in section 4.2 of Part 1). This implies that the observational filtering is not the only factor for the relatively short vertical wavelength GWs observed in the present study. The wave properties also seem to vary with season rather than with the sources, although the numbers of waves in each season are different. This implies that the background atmosphere significantly affects the characteristics of GWs during their propagation to observed altitude. This is confirmed from Figure 11, which describes the vertical profiles of background wind projected to the horizontal wavenumber vector ($V_{proj} = \vec{V} \cdot \vec{k_h} / \left| \vec{k_h} \right|$, where k_h is the horizontal wavenumber vector), square of buoyancy frequency, vertical wavelength, and horizontal wavelength following the rays of the observed waves from different sources. The horizontal wavelengths mostly do not vary following rays, whereas the vertical wavelengths of the tropospheric GWs change significantly during their propagation (Figures 11a–11c). Those behaviors have also been identified from the ray tracing analysis in Ki and Chun (2011). They inferred that the horizontal wavenumber ($k_h = 2\pi/\lambda_h$) of the waves tends to be determined predominantly by the source, while the vertical wavenumber ($m = 2\pi/\lambda_z$) changes significantly during propagation because the vertical wavenumber is mainly determined by V_{proj} and the buoyancy frequency for a given horizontal wavenumber following the dispersion relationship of the IGWs. The vertical wavelength of the GWs originated in the troposphere tended to have the maximum with the smallest static stability and the largest magnitude of negative V_{proj} and then decreased with height due to the increasing stability and decreasing magnitude of negative V_{proj} in the stratosphere. Therefore, the seasonal variations revealed in the properties of GWs at the time of observation are attributed to the seasonal variabilities in V_{proj} and the stability of the background atmosphere in the stratosphere.

4.3.2. Phase Velocities and their Relation to the Background Wind

Figure 12 illustrates the ground-based phase velocities of the GWs generated by individual sources in each season when those waves are excited (upper panel) and observed from the radiosonde (lower panel). Orographic GWs exhibit an isotropic distribution of phase velocity with speeds of less than 10 m s^{-1} at the time of generation, reflecting the criterion used for identifying the orographic GWs (Figure 12a). On the other hand, GWs associated with fronts and convection propagate more eastward at a speed of less than 30 m s^{-1} (Figures 12b and 12c). GWs generated by the flow imbalance have dominant eastward phase velocities with wider speed ranges of up to 60 m s^{-1} (Figure 12d). The horizontal phase velocities of the GWs at the time of observation exhibit similar speed ranges to those of the GWs at the time of generation. Obvious seasonal variations appear in the phase velocities when they are generated as well as when they are observed: higher speeds from autumn to spring in comparison to lower speeds in summer. This feature resembles the seasonal variations in the background wind, which are enhanced from late autumn to early spring and weakened during summer.
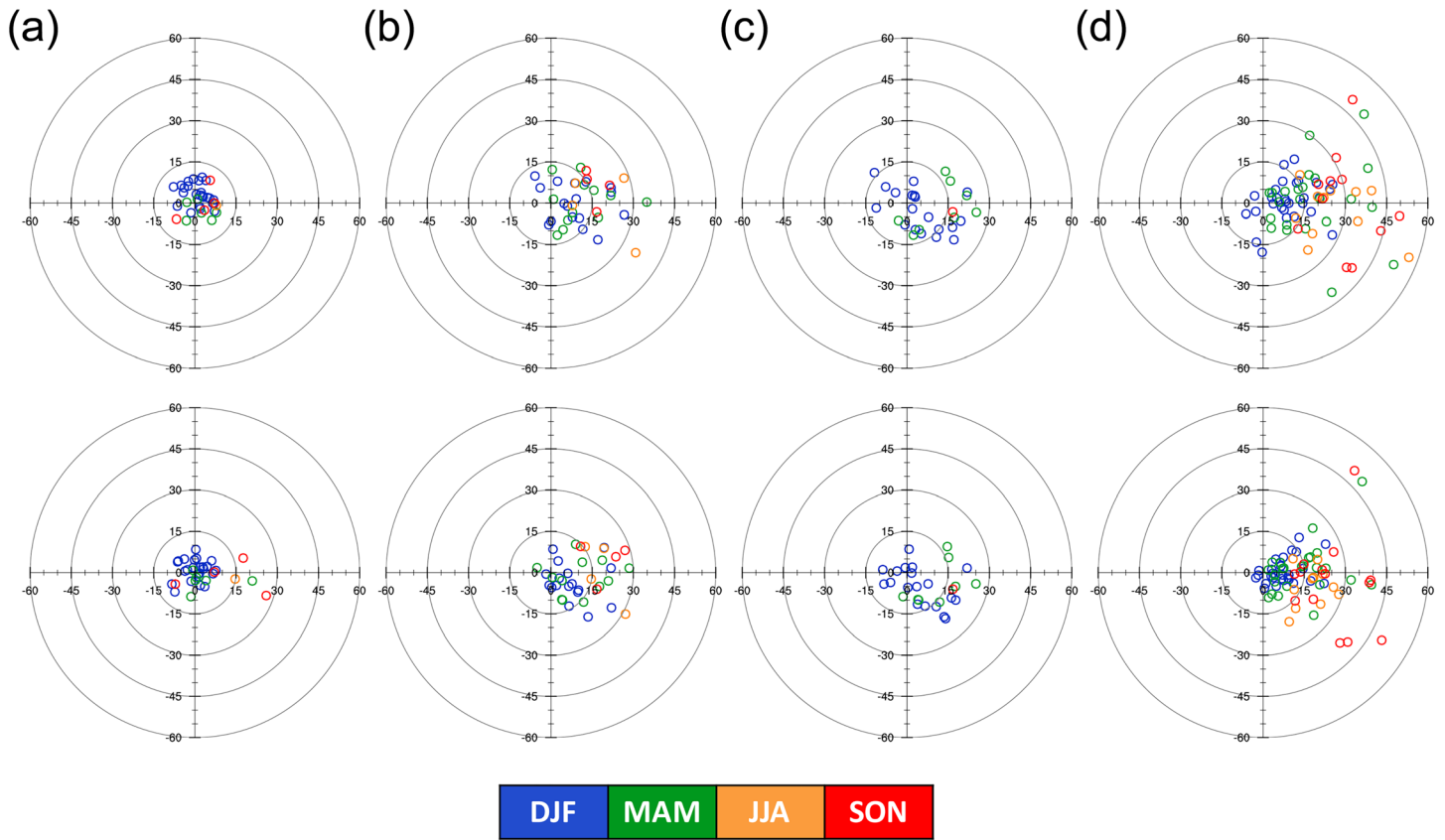
Figure 11. Profiles of background wind projected to the horizontal wavenumber vector (first column), square of buoyancy frequency (second column), vertical wavelength (third column), and horizontal wavelength (fourth column) following the rays of observed waves that originate from (a) orography, (b) surface front, (c) convection, and (d) flow imbalance. The colors of the lines represent the seasons in which each wave is observed. Cyan, purple, red, and orange correspond to summer, autumn, winter, and spring, respectively.

5. Summary and Conclusion

In the present study, the potential sources of the IGWs in the lower stratosphere ($z = 15–22$ km) revealed in the radiosonde observations at Jang Bogo Station (JBS; 74°37′S, 164°13′E) are investigated. Analyses are performed using the characteristics of IGWs extracted from 3 years of radiosonde data (December 2014 to November 2017), including the 25-month (from December 2014 to December 2016) data used in Yoo et al. (2018; Part 1). Wave parameters obtained from the 3-year period radiosonde data exhibit similar values to those reported in Part 1: The average values of the intrinsic frequency, vertical wavelength, and horizontal wavelength are $2.04f$, 1.47 km, and 217 km, respectively, and those of kinetic and potential energies are 3.28 and 1.11 J kg^{-1}, respectively. Pronounced northeast and southeastward phase velocities and group velocities with a maximum speed of 80 m s^{-1} also agree with the result in Part 1. Potential effects of the observational filter and analysis methods on the characteristics of IGWs are discussed in more detail in Part 1.

Using the wave parameters estimated from the radiosonde data, the three-dimensional backward ray tracing calculation is conducted by applying the GROGRAT model to locate the source regions for the observed IGWs. Of the 248 IGWs, the largest number of waves (112; 45%) are traced down to the troposphere ($z < 8$ km), whereas 68 (27.5%) and 68 (27.5%) waves are traceable to the tropopause ($z = 8–15$ km) and stratosphere ($z = 15–18.5$ km), respectively. Here, we assume that the wave generation occurs in a certain horizontal (the spherical area corresponding to the area of a circle with radius R corresponding to a distance of 3° in latitude) and vertical area ($z = \pm 2$ km) from the termination position of the ray, within 3 hr around the wave generation time inferred from the backward ray tracing time. Most of IGWs generated in the troposphere have their sources along the longitudinal region of 90°E to 180° over the Southern Indian Ocean
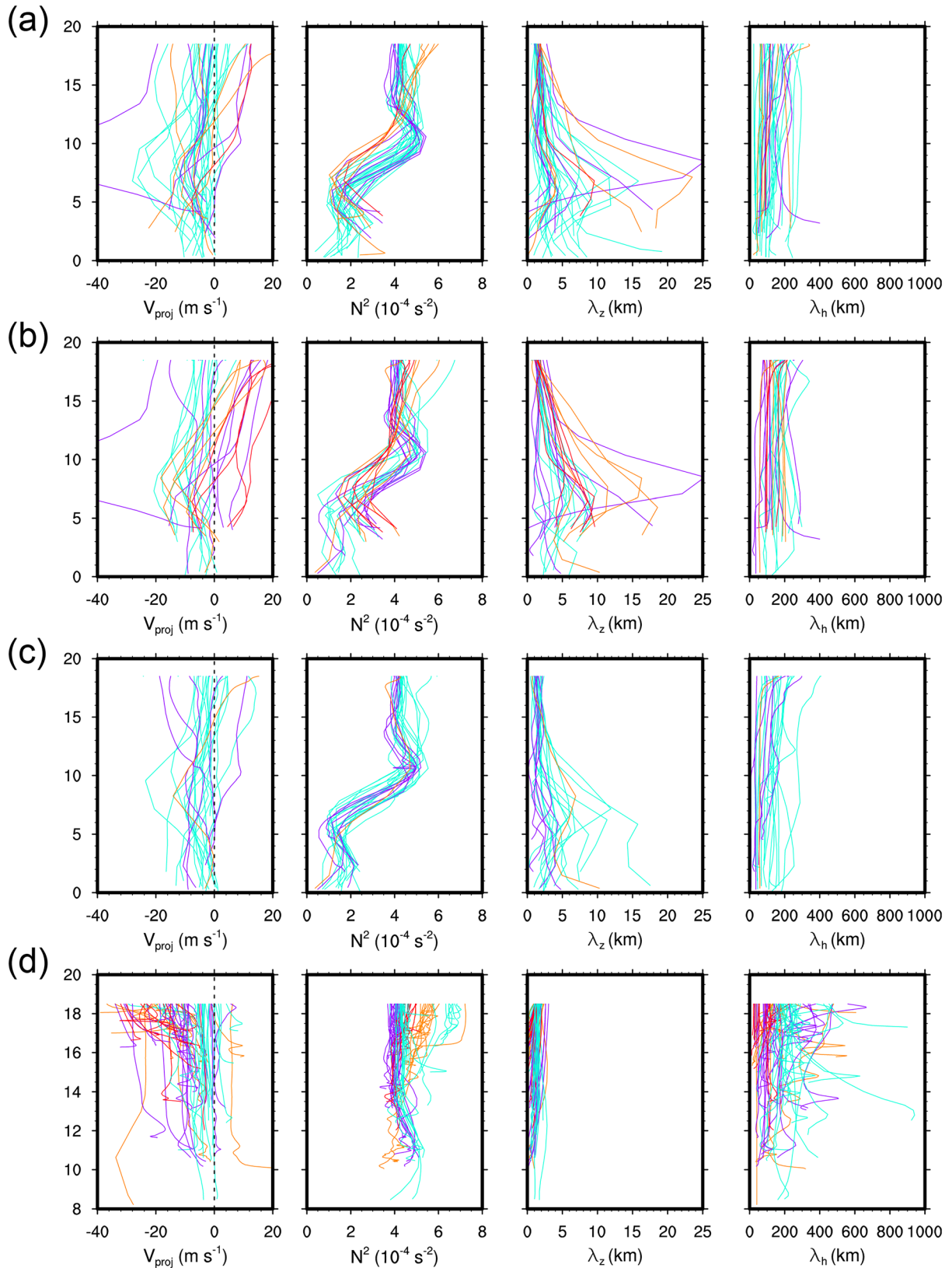
Figure 12. Distribution of the phase velocities for each wave associated with (a) orography, (b) surface front, (c) convection, and (d) flow imbalance at the time of generation (upper panel) and observation (lower panel). The colors of the circles represent the seasons in which each wave is observed. Blue, green, orange, and red correspond to summer, autumn, winter, and spring, respectively. Right and upward directions indicate eastward and northward directions, respectively.

(70–45°S) as well as above the Antarctic continent and Ross Sea. In the tropopause and stratosphere, waves are mostly excited in the higher southern latitudes (poleward of 50°S) and over all longitudes. These waves mainly propagate from the northwestern and southwestern regions of JBS affected by the prevailing wester-lies between the upper troposphere and the lower stratosphere.

Based on the ray tracing analysis, we made attempt to identify the potential sources of the IGWs: orography, fronts, convection, and the flow imbalance including upper-tropospheric jet stream. To diagnose wave generation by the proposed sources, appropriate indicators (the topographic slope and ground-based phase velocity for the orographic GWs, FF for the frontal GWs, hourly precipitation for the convective GWs, and |RNBE| for the GWs associated with the imbalanced flow) and their threshold values are determined. In addition, we briefly assess whether GWs associated with these sources actually appear in the high-resolution ERA5 reanalysis data. In ERA 5, GWs associated with the probable sources are represented well, but all the detailed quantitative properties of GW estimated from GROGRAT cannot be precisely reproduced.

Applying the diagnostic methods, we categorize the observed IGWs into the waves generated by the aforementioned sources. Among the 112 waves generated in the troposphere, 37 (33%), 35 (31%), and 28 (25%) waves are categorized as the waves induced by the fronts, orography, and convection, respectively. The number of waves induced by the flow imbalance in the tropopause and stratosphere are 42 (61%) and 36 (52%) out of the total 68 and 68 waves, respectively. Of the 36 waves generated by the flow imbalance in the tropopause region, 11 waves (30%) are associated with the tropopause jet stream. However, the probable source is not identified for a large number of waves (35, 32, and 28 waves in the troposphere, tropopause, and stratosphere, respectively), suggesting that other potential sources may exist in addition to the four major sources. It is also possible that GW generation by the given four sources could have occurred somewhere in the ray path before they are terminated. It is noteworthy that the temporal variations in the mean flow and resultant frequency change following rays had not been considered in the GROGRAT used for the present study. As time limitation of ray tracing calculation set to 5 days in the present study, changes in the mean flow may influence on the ray termination position and consequent source categorization. The impacts of the time-dependent mean flow to the ray tracing calculation of the current study remain for the future research.

The locations of wave generation and corresponding propagations of the waves toward JBS are remarkably different depending on the sources. Most of the orographic GWs originate from the western coastal regions of the Ross Sea, where steep terrain slopes exist. On the other hand, many of the convective GWs and frontal GWs are generated from the Southern Indian Ocean (50–60°S), which has been recognized as the active nonorographic GW region (Hendricks et al., 2014). These waves propagate long horizontal distances to JBS at higher southern latitudes, which is similar to the lateral propagation of GWs excited in the SH storm track regions in Choi and Chun (2013). The waves associated with the flow imbalance in the tropopause and stratosphere mainly originate in the entire longitudes at the higher southern latitudes (poleward of 50°S) and predominantly travel horizontally rather than vertically. Pronounced horizontal propagations of the nonorographic GWs elucidates the need for ray theory in the GWD parameterizations in GCM to better represent the GW effect. Meanwhile, most of the orographic GWs and convective GWs are generated during summertime, whereas the GWs associated with fronts and the flow imbalance are excited without obvious seasonal variations. For the lack of orographic GWs during wintertime, which is different from the predominant wave generation in wintertime in Watanabe et al. (2006), the observational filtering of the long vertical wavelength of GWs by the Doppler shifting effect is suggested as the main factor, in addition to too small number of radiosonde profiles (7) available in the lower stratosphere in the wintertime due to the extremely cold temperature at JBS. On the other hand, the seasonal and geographical variations in the emission of nonorographic GWs are found to be closely related to those variabilities in the nonorographic source itself.

Finally, we investigate characteristics of IGWs with respect to their potential sources at the time of wave generation estimated from GROGRAT and the time of observation. At the time of wave generation, the waves of tropospheric origins have wider ranges of intrinsic frequency (1–20f) and vertical wavelength (0.5–10 km), whereas the waves induced by the imbalanced flow exhibit a predominantly low intrinsic frequency (less than 2f) and short vertical wavelength (less than 3 km). However, the waves generated by the

tropospheric sources as well as by the flow imbalance in the tropopause and stratosphere have similar characteristics at the observation altitude that are low intrinsic frequency (less than $4f$), short vertical wavelength (less than 3 km), and relatively longer horizontal wavelength (less than 1,000 km). This implies that GWs experience significant modifications by the background atmosphere during their propagation. The ground-based phase velocities between the time of generation and observation exhibit similar distributions: Orographic GWs have isotropic distributions with speeds of less than 10 m s^{-1}, whereas GWs generated by fronts and convection exhibit more eastward phase velocities than westward GWs with speeds of up to 30 m s^{-1}. GWs induced by the flow imbalance have predominantly eastward phase velocities with a maximum wind speed of up to 60 m s^{-1}. Not only when they are observed but also when they are generated, obvious seasonal variations in the phase velocities are identified, which resemble the variations in the background wind that are enhanced (reduced) between late autumn and early spring (during summer).

Appendix A: Ray Tracing Equations

The governing equations of the GROGRAT ray tracer are as follows (Lighthill, 1978):

$$\frac{dx_i}{dt} = C_{gx_i} = \frac{\partial \omega}{\partial k_i} \ (i = 1, 2, 3), \tag{A1}$$

$$\frac{dk_i}{dt} = -\frac{\partial \omega}{\partial x_i} \qquad (i = 1, 2, 3), \tag{A2}$$

where $(x_1, x_2, x_3) = (x, y, z)$ are the wave packet position and $(k_1, k_2, k_3) = (k, l, m)$ are the zonal, meridional, and vertical wavenumbers; ω is the ground-based frequency, and $(C_{gx}, C_{gy}, C_{gz}) = \left(\frac{\partial \omega}{\partial k}, \frac{\partial \omega}{\partial l}, \frac{\partial \omega}{\partial m}\right)$ are the zonal, meridional, and vertical components of the ground-based group velocity, respectively. The model is based on the dispersion relation for nonhydrostatic IGWs on a slowly varying basic flow:

$$\widehat{\omega}^2 = (\omega - Uk - Vl)^2 = \frac{N^2\left(k^2 + l^2\right) + f^2\left(m^2 + \alpha^2\right)}{k^2 + l^2 + m^2 + \alpha^2}. \tag{A3}$$

Here, U and V are the zonal and meridional basic-state winds, respectively, N is the buoyancy frequency, and $\alpha^2 = 1/(2H)^2$, where H is the density scale-height. Using A3, the governing equations A1 and A2 are expressed as

$$\frac{dx}{dt} = C_{gx} = \frac{\partial \omega}{\partial k} = U + \frac{k(N^2 - \widehat{\omega}^2)}{\widehat{\omega}\sigma^2}, \tag{A4}$$

$$\frac{dy}{dt} = C_{gy} = \frac{\partial \omega}{\partial l} = V + \frac{l(N^2 - \widehat{\omega}^2)}{\widehat{\omega}\sigma^2}, \tag{A5}$$

$$\frac{dz}{dt} = C_{gz} = \frac{\partial \omega}{\partial m} = -\frac{m\left(\widehat{\omega}^2 - f^2\right)}{\widehat{\omega}\sigma^2}, \tag{A6}$$

$$\frac{dk}{dt} = -\frac{\partial \omega}{\partial x} = -k\frac{\partial U}{\partial x} - l\frac{\partial V}{\partial x} - \frac{1}{2\widehat{\omega}\sigma^2}\left[\frac{\partial N^2}{\partial x}\left[k^2 + l^2\right] - \frac{\partial \alpha^2}{\partial x}\left[\widehat{\omega}^2 - f^2\right]\right], \tag{A7}$$

$$\frac{dl}{dt} = -\frac{\partial \omega}{\partial y} = -k\frac{\partial U}{\partial y} - l\frac{\partial V}{\partial y} - \frac{1}{2\widehat{\omega}\sigma^2}\left[\frac{\partial N^2}{\partial y}\left[k^2 + l^2\right] - \frac{\partial \alpha^2}{\partial y}\left[\widehat{\omega}^2 - f^2\right] + \frac{\partial f^2}{\partial y}\left[m^2 + \alpha^2\right]\right], \tag{A8}$$

$$\frac{dm}{dt} = -\frac{\partial \omega}{\partial z} = -k\frac{\partial U}{\partial z} - l\frac{\partial V}{\partial z} - \frac{1}{2\widehat{\omega}\sigma^2}\left[\frac{\partial N^2}{\partial z}\left[k^2 + l^2\right] - \frac{\partial \alpha^2}{\partial z}\left[\widehat{\omega}^2 - f^2\right]\right], \tag{A9}$$

where $\sigma^2 = k^2 + l^2 + m^2 + \alpha^2$.

The standard version of GROGRAT uses the Cartesian coordinate system. In the spherical coordinates, the evolution of wave number components is determined not only by the changes in the wave number vector but also the spatial variation of the coordinate frame. Therefore, as proposed by Hasha et al. (2008), the standard version was extended to the spherical geometry by correcting the refraction of the wave

vector (Kalisch et al., 2014). Given the wave number vector denoted as $\vec{k} = k\hat{\lambda} + l\hat{\theta} + m\hat{r}$, where $\hat{\lambda}$, $\hat{\theta}$, and $\hat{r}$ are zonal, meridional, and radial unit vectors, respectively, the spatial variations of the coordinate frame are

$$\frac{d\lambda}{dt} = \frac{1}{r\cos\theta}\left[U + \frac{k[N^2 - \hat{\omega}^2]}{\hat{\omega}\sigma^2}\right], \tag{A10}$$

$$\frac{dy}{dt} = \frac{1}{r}\left[V + \frac{l[N^2 - \hat{\omega}^2]}{\hat{\omega}\sigma^2}\right], \tag{A11}$$

$$\frac{dr}{dt} = -\frac{m(\hat{\omega}^2 - f^2)}{\hat{\omega}\sigma^2}. \tag{A12}$$

Then, the refraction of the wave vector in the spherical coordinate system can be rewritten as

$$\frac{dk}{dt} = -\frac{k}{r\cos\theta}\frac{\partial U}{\partial\lambda} - \frac{l}{r\cos\theta}\frac{\partial V}{\partial\lambda} - \frac{1}{2\hat{\omega}\sigma^2}\left[\frac{k^2 + l^2}{r\cos\theta}\frac{\partial N^2}{\partial\lambda} - \frac{[\hat{\omega}^2 - f^2]}{r\cos\theta}\frac{\partial\alpha^2}{\partial x}\right] - \frac{k}{r}\frac{dr}{dt} + k\tan\theta\frac{d\theta}{dt}, \tag{A13}$$

$$\frac{dl}{dt} = -\frac{k}{r}\frac{\partial U}{\partial y} - \frac{l}{r}\frac{\partial V}{\partial y} - \frac{1}{2\hat{\omega}\sigma^2}\left[\frac{(k^2 + l^2)}{r}\frac{\partial N^2}{\partial\theta} - \frac{(\hat{\omega}^2 - f^2)}{r}\frac{\partial\alpha^2}{\partial\theta} - \frac{(m^2 + \alpha^2)}{r}\frac{\partial f^2}{\partial\theta}\right] - \frac{l}{r}\frac{dr}{dt} - k\sin\theta\frac{d\lambda}{dt}, \tag{A14}$$

$$\frac{dm}{dt} = -k\frac{\partial U}{\partial r} - l\frac{\partial V}{\partial r} - \frac{1}{2\hat{\omega}\sigma^2}\left[(k^2 + l^2)\frac{\partial N^2}{\partial r} - (\hat{\omega}^2 - f^2)\frac{\partial\alpha^2}{\partial r}\right] + l\frac{d\theta}{dt} + k\cos\theta\frac{d\lambda}{dt}. \tag{A15}$$

References

Alexander, M. J. (1998). Interpretations of observed climatological patterns in stratospheric gravity wave variance. *Journal of Geophysical Research*, *103*(D8), 8627–8640. https://doi.org/10.1029/97JD03325

Alexander, M. J., Eckermann, S. D., Broutman, D., & Ma, J. (2009). Momentum flux estimates for South Georgia Island mountain waves in the stratosphere observed via satellite. *Geophysical Research Letters*, *36*, L12816. https://doi.org/10.1029/2009GL038587

Alexander, M. J., & Grimsdell, A. W. (2013). Seasonal cycle of orographic gravity wave occurrence above small islands in the Southern Hemisphere: Implications for effects on the general circulation. *Journal of Geophysical Research: Atmospheres*, *118*, 11–589. https://doi.org/10.1002/2013JD020526

Alexander, M. J., & Teitelbaum, H. (2011). Three-dimensional properties of Andes mountain waves observed by satellite: A case study. *Journal of Geophysical Research*, *116*, D23110. https://doi.org/10.1029/2011JD016151

Alexander, S. P., Klekociuk, A. R., McDonald, A. J., & Pitts, M. C. (2013). Quantifying the role of orographic gravity waves on polar stratospheric cloud occurrence in the Antarctic and the Arctic. *Journal of Geophysical Research*, *118*, 11,493–11,507. https://doi.org/10.1002/2013jd020122

Amante, C., & Eakins, B. W. (2009). ETOPO1 arc-minute global relief model: Procedures, data sources and analysis.

Baumgaertner, A. J. G., & McDonald, A. J. (2007). A gravity wave climatology for Antarctica compiled from Challenging Minisatellite Payload/Global Positioning System (CHAMP/GPS) radio occultations. *Journal of Geophysical Research*, *112*, D05103. https://doi.org/10.1029/2006JD007504

Charron, M., & Manzini, E. (2002). Gravity waves from fronts: Parameterization and middle atmosphere response in a general circulation model. *Journal of the Atmospheric Sciences*, *59*(5), 923–941. https://doi.org/10.1175/1520-0469(2002)059<0923:GWFFPA>2.0.CO;2

Choi, H.-J., & Chun, H.-Y. (2013). Effects of convective gravity wave drag in the Southern Hemisphere winter stratosphere. *Journal of the Atmospheric Sciences*, *70*(7), 2120–2136. https://doi.org/10.1175/JAS-D-12-0238.1

Choi, H. J., Han, J. Y., Koo, M. S., Chun, H. Y., Kim, Y. H., & Hong, S. Y. (2018). Effects of non-orographic gravity wave drag on seasonal and medium-range predictions in a global forecast model. *Asia-Pacific Journal of Atmospheric Sciences*, *54*(1), 385–402. https://doi.org/10.1007/s13143-018-0023-1

Chun, H. Y., Goh, J. S., & Kim, Y. H. (2007). Characteristics of inertio-gravity waves revealed in rawinsonde data observed in Korea during 20 August to 5 September 2002. *Journal of Geophysical Research*, *112*, D16108. https://doi.org/10.1029/2006JD008348

Chun, H. Y., Song, B. G., Shin, S. W., & Kim, Y. H. (2019). Gravity waves associated with jet/front systems. Part I: Diagnostics and their correlations with GWs revealed in high-resolution global analysis data. *Asia-Pacific Journal of Atmospheric Sciences*, *55*(4), 589–608. https://doi.org/10.1007/s13143-019-00104-1

Chun, H. Y., Song, I. S., & Baik, J. J. (2006). Seasonal variations of gravity waves revealed in rawinsonde data at Pohang, Korea. *Meteorology and Atmospheric Physics*, *93*(3–4), 255–273. https://doi.org/10.1007/s00703-005-0164-5

Dee, D. P., Uppala, S. M., Simmons, A. J., Berrisford, P., Poli, P., Kobayashi, S., et al. (2011). The ERA-Interim reanalysis: Configuration and performance of the data assimilation system. *Quarterly Journal of the Royal Meteorological Society*, *137*(656), 553–597. https://doi.org/10.1002/qj.828

Eckermann, S. D., & Marks, C. J. (1997). GROGRAT: A new model of the global propagation and dissipation of atmospheric gravity waves. *Advances in Space Research*, *20*(6), 1253–1256. https://doi.org/10.1016/S0273-1177(97)00780-1

Eckermann, S. D., & Vincent, R. A. (1993). VHF radar observations of gravity-wave production by cold fronts over southern Australia. *Journal of the Atmospheric Sciences*, *50*(6), 785–806. https://doi.org/10.1175/1520-469(1993)050<0785:VROOGW>2.0.CO;2

Ern, M., Preusse, P., Alexander, M. J., & Warner, C. D. (2004). Absolute values of gravity wave momentum flux derived from satellite data. *Journal of Geophysical Research*, *109*, D20103. https://doi.org/10.1029/2004JD004752

Ern, M., Preusse, P., Gille, J. C., Hepplewhite, C. L., Mlynczak, M. G., Russell, J. M. III, & Riese, M. (2011). Implications for atmospheric dynamics derived from global observations of gravity wave momentum flux in stratosphere and mesosphere. *Journal of Geophysical Research*, *116*, D19107. https://doi.org/10.1029/2011JD015821

Evan, S., Alexander, M. J., & Dudhia, J. (2012). Model study of intermediate-scale tropical inertia–gravity waves and comparison to TWP-ICE campaign observations. *Journal of the Atmospheric Sciences*, *69*(2), 591–610. https://doi.org/10.1175/JAS-D-11-051.1

Fritts, D. C., & Alexander, M. J. (2003). Gravity wave dynamics and effects in the middle atmosphere. *Reviews of Geophysics*, *41*(1), 1003. https://doi.org/10.1029/2001RG000106

Fritts, D. C., & Nastrom, G. D. (1992). Sources of mesoscale variability of gravity waves. Part II: Frontal, convective, and jet stream excitation. *Journal of the Atmospheric Sciences*, *49*(2), 111–127. https://doi.org/10.1175/1520-0469(1992)049<0111:SOMVOG>2.0.CO;2

Gallego, D., Ribera, P., Garcia-Herrera, R., Hernandez, E., & Gimeno, L. (2005). A new look for the Southern Hemisphere jet stream. *Climate Dynamics*, *24*(6), 607–621. https://doi.org/10.1007/s00382-005-0006-7

Garcia, R. R., & Boville, B. A. (1994). "Downward control" of the mean meridional circulation and temperature distribution of the polar winter stratosphere. *Journal of the Atmospheric Sciences*, *51*(15), 2238–2245. https://doi.org/10.1175/1520-0469(1994)051<2238:COTMMC>2.0.CO;2

Garcia, R. R., Smith, A. K., Kinnison, D. E., Cámara, Á. D. L., & Murphy, D. J. (2017). Modification of the gravity wave parameterization in the Whole Atmosphere Community Climate Model: Motivation and results. *Journal of the Atmospheric Sciences*, *74*(1), 275–291. https://doi.org/10.1175/JAS-D-16-0104.1

Geller, M. A., Alexander, M. J., Love, P. T., Bacmeister, J., Ern, M., Hertzog, A., et al. (2013). A comparison between gravity wave momentum fluxes in observations and climate models. *Journal of Climate*, *26*(17), 6383–6405. https://doi.org/10.1175/JCLI-D-12-00545.1

Griffiths, M., & Reeder, M. J. (1996). Stratospheric inertia–gravity waves generated in a numerical model of frontogenesis. I: Model solutions. *Quarterly Journal of the Royal Meteorological Society*, *122*(533), 1153–1174. https://doi.org/10.1002/qj.49712253307

Guest, F. M., Reeder, M. J., Marks, C. J., & Karoly, D. J. (2000). Inertia–gravity waves observed in the lower stratosphere over Macquarie Island. *Journal of the Atmospheric Sciences*, *57*(5), 737–752. https://doi.org/10.1175/1520-469(2000)057<0737:IGWOIT>2.0.CO;2

Hasha, A., Bühler, O., & Scinocca, J. (2008). Gravity wave refraction by three-dimensionally varying winds and the global transport of angular momentum. *Journal of the Atmospheric Sciences*, *65*(9), 2892–2906. https://doi.org/10.1175/2007JAS2561.1

Hendricks, E. A., Doyle, J. D., Eckermann, S. D., Jiang, Q., & Reinecke, P. A. (2014). What is the source of the stratospheric gravity wave belt in austral winter? *Journal of the Atmospheric Sciences*, *71*(5), 1583–1592. https://doi.org/10.1175/JAS-D-13-0332.1

Hersbach, H., & Dee, D. (2016). ERA5 reanalysis is in production. In *ECMWF Newsletter* (Vol. 147, p. 7). UK: Reading. Retrieved from https://www.ecmwf.int/en/newsletter/147/news/era5-reanalysis-production

Hertzog, A., Boccara, G., Vincent, R. A., Vial, F., & Cocquerez, P. (2008). Estimation of gravity wave momentum flux and phase speeds from quasi-Lagrangian stratospheric balloon flights. Part II: Results from the Vorcore campaign in Antarctica. *Journal of the Atmospheric Sciences*, *65*(10), 3056–3070. https://doi.org/10.1175/2008JAS2710.1

Hertzog, A., Souprayen, C., & Hauchecorne, A. (2001). Observation and backward trajectory of an inertio-gravity wave in the lower stratosphere. In. *Annales Geophysicae*, *19*(9), 1141–1155. https://doi.org/10.5194/angeo-19-1141-2001

Hoffmann, L., Günther, G., Li, D., Stein, O., Wu, X., Griessbach, S., et al. (2019). From ERA-Interim to ERA5: The considerable impact of ECMWF's next-generation reanalysis on Lagrangian transport simulations. *Atmospheric Chemistry and Physics*, *19*(5), 3097–3124. https://doi.org/10.5194/acp-19-3097-2019

Hoffmann, L., Xue, X., & Alexander, M. J. (2013). A global view of stratospheric gravity wave hotspots located with Atmospheric Infrared Sounder observations. *Journal of Geophysical Research: Atmospheres*, *118*, 416–434. https://doi.org/10.1029/2012JD018658

Holt, L. A., Alexander, M. J., Coy, L., Liu, C., Molod, A., Putman, W., & Pawson, S. (2017). An evaluation of gravity waves and gravity wave sources in the Southern Hemisphere in a 7 km global climate simulation. *Quarterly Journal of the Royal Meteorological Society*, *143*(707), 2481–2495. https://doi.org/10.1002/qj.3101

Hoskins, B. J. (1982). The mathematical theory of frontogenesis. *Annual Review of Fluid Mechanics*, *14*(1), 131–151.

Hoskins, B. J., & Hodges, K. I. (2005). A New Perspective on Southern Hemisphere Storm Tracks. *Journal of Climate*, *18*(20), 4108–4129. https://doi.org/10.1175/jcli3570.1

Huffman, G. J., Bolvin, D. T., Stocker, E. F., & Tan, J. (2017). V05 IMERG final run release notes (5 pp.). Retrieved from https://pps.gsfc.nasa.gov/Documents/IMERG_FinalRun_V05_release_notes-rev03.pdf

Kalisch, S., Preusse, P., Ern, M., Eckermann, S. D., & Riese, M. (2014). Differences in gravity wave drag between realistic oblique and assumed vertical propagation. *Journal of Geophysical Research: Atmospheres*, *119*, 10–081. https://doi.org/10.1002/2014JD021779

Kang, M. J., Chun, H. Y., & Kim, Y. H. (2017). Momentum flux of convective gravity waves derived from an offline gravity wave parameterization. Part I: Spatiotemporal variations at source level. *Journal of the Atmospheric Sciences*, *74*(10), 3167–3189. https://doi.org/10.1175/JAS-D-17-0053.1

Ki, M. O., & Chun, H. Y. (2011). Inertia gravity waves associated with deep convection observed during the summers of 2005 and 2007 in Korea. *Journal of Geophysical Research*, *116*, D16122. https://doi.org/10.1029/2011JD015684

Ki, M. -O., & Chun, H. -Y. (2010). Characteristics and sources of inertia-gravity waves revealed in the KEOP-2007 radiosonde data. *Asia-Pacific Journal of Atmospheric Sciences*, *46*(3), 261–277. https://doi.org/10.1007/s13143-010-1001-4

Kim, J. H., Chun, H. Y., Sharman, R. D., & Keller, T. L. (2011). Evaluations of upper-level turbulence diagnostics performance using the Graphical Turbulence Guidance (GTG) system and pilot reports (PIREPs) over East Asia. *Journal of Applied Meteorology and Climatology*, *50*(9), 1936–1951. https://doi.org/10.1175/JAMC-D-10-05017.1

Kim, Y. H., Chun, H. Y., Park, S. H., Song, I. S., & Choi, H. J. (2016). Characteristics of gravity waves generated in the jet-front system in a baroclinic instability simulation. *Atmospheric Chemistry and Physics*, *16*, 4799–4815. https://doi.org/10.5194/acp-16-4799-2016

Kim, Y. -J., Eckermann, S. D., & Chun, H. -Y. (2003). An overview of the past, present and future of gravity-wave drag parametrization for numerical climate and weather prediction models. *Atmosphere-Ocean*, *41*(1), 65–98. https://doi.org/10.3137/ao.410105

Lighthill, J. (1978). *Waves in fluids*. Cambridge: Cambridge University Press.

Limpasuvan, V., Alexander, M. J., Orsolini, Y. J., Wu, D. L., Xue, M., Richter, J. H., & Yamashita, C. (2011). Mesoscale simulations of gravity waves during the 2008–2009 major stratospheric sudden warming. *Journal of Geophysical Research*, *116*, D17104. https://doi.org/10.1029/3010JD015190

Lin, Y., & Zhang, F. (2008). Tracking gravity waves in baroclinic jet-front systems. *Journal of the Atmospheric Sciences*, *65*(7), 2402–2415. https://doi.org/10.1175/2007JAS2482.1

Lindzen, R. S. (1981). Turbulence and stress owing to gravity wave and tidal breakdown. *Journal of Geophysical Research*, *86*(C10), 9707–9714. https://doi.org/10.1029/JC086iC10p09707

Marks, C. J., & Eckermann, S. D. (1995). A three-dimensional nonhydrostatic ray-tracing model for gravity waves: Formulation and preliminary results for the middle atmosphere. *Journal of the Atmospheric Sciences*, *52*(11), 1959–1984. https://doi.org/10.1175/1520-0469(1995)052<1959:ATDNRT>2.0.CO;2

McLandress, C., Alexander, M. J., & Wu, D. L. (2000). Microwave Limb Sounder observations of gravity waves in the stratosphere: A climatology and interpretation. *Journal of Geophysical Research*, *105*(D9), 11,947–11,967.

McLandress, C., Shepherd, T. G., Polavarapu, S., & Beagley, S. R. (2012). Is missing orographic gravity wave drag near 60°S the cause of the stratospheric zonal wind biases in chemistry–climate models? *Journal of the Atmospheric Sciences*, *69*(3), 802–818. https://doi.org/10.1175/JAS-D-11-0159.1

Miller, J. E. (1948). On the concept of frontogenesis. *Journal of Meteorology*, *5*(4), 169–171. https://doi.org/10.1175/1520-0469(1948)005<0169:OTCOF>2.0.CO;2

Murphy, D. J., Alexander, S. P., Klekociuk, A. R., Love, P. T., & Vincent, R. A. (2014). Radiosonde observations of gravity waves in the lower stratosphere over Davis, Antarctica. *Journal of Geophysical Research: Atmospheres*, *119*, 11–973. https://doi.org/10.1002/2014JD022448

O'sullivan, D., & Dunkerton, T. J. (1995). Generation of inertia–gravity waves in a simulated life cycle of baroclinic instability. *Journal of the Atmospheric Sciences*, *52*(21), 3695–3716. https://doi.org/10.1175/1520-0469(1995)052<3695:GOIWIA>2.0.CO;2

Plougonven, R., Hertzog, A., & Guez, L. (2013). Gravity waves over Antarctica and the Southern Ocean: Consistent momentum fluxes in mesoscale simulations and stratospheric balloon observations. *Quarterly Journal of the Royal Meteorological Society*, *139*(670), 101–118. https://doi.org/10.1002/qj.1965

Plougonven, R., Jewtoukoff, V., Cámara, A. D. L., Lott, F., & Hertzog, A. (2017). On the relation between gravity waves and wind speed in the lower stratosphere over the Southern Ocean. *Journal of the Atmospheric Sciences*, *74*(4), 1075–1093. https://doi.org/10.1175/JAS-D-16-0096.1

Plougonven, R., & Snyder, C. (2007). Inertia–gravity waves spontaneously generated by jets and fronts. Part I: Different baroclinic life cycles. *Journal of the Atmospheric Sciences*, *64*(7), 2502–2520. https://doi.org/10.1175/JAS3953.1

Plougonven, R., & Teitelbaum, H. (2003). Comparison of a large-scale inertia-gravity wave as seen in the ECMWF analyses and from radiosondes. *Geophysical Research Letters*, *30*(18), 1954. https://doi.org/10.1029/2003GL017716

Plougonven, R., & Zhang, F. (2014). Internal gravity waves from atmospheric jets and fronts. *Reviews of Geophysics*, *52*(1), 33–76. https://doi.org/10.1002/2012RG000419

Pramitha, M., Ratnam, M. V., Leena, P. P., Murthy, B. K., & Rao, S. V. B. (2016). Identification of inertia gravity wave sources observed in the troposphere and the lower stratosphere over a tropical station Gadanki. *Atmospheric Research*, *176*, 202–211. https://doi.org/10.1016/j.atmosres.2016.03.001

Pramitha, M., Venkat Ratnam, M., Taori, A., Krishna Murthy, B. V., Pallamraju, D., & Vijaya Bhaskar Rao, S. (2015). Evidence for tropospheric wind shear excitation of high-phase-speed gravity waves reaching the mesosphere using the ray-tracing technique. *Atmospheric Chemistry and Physics*, *15*(5), 2709–2721. https://doi.org/10.5194/acp-15-2709-2015

Preusse, P., Dörnbrack, A., Eckermann, S. D., Riese, M., Schaeler, B., Bacmeister, J. T., et al. (2002). Space-based measurements of stratospheric mountain waves by CRISTA 1. Sensitivity, analysis method, and a case study. *Journal of Geophysical Research*, *107*(D23), 8178. https://doi.org/10.1029/2001JD000699

Preusse, P., Ern, M., Bechtold, P., Eckermann, S. D., Kalisch, S., Trinh, Q. T., & Riese, M. (2014). Characteristics of gravity waves resolved by ECMWF. *Atmospheric Chemistry and Physics*, *14*(19), 10,483–10,508. https://doi.org/10.5194/acp-14-10483-2014

Reeder, M. J., & Griffiths, M. (1996). Stratospheric inertia–gravity waves generated in a numerical model of frontogenesis. II: Wave sources, generation mechanisms and momentum fluxes. *Quarterly Journal of the Royal Meteorological Society*, *122*(533), 1175–1195. https://doi.org/10.1002/qj.49712253308

Richter, J. H., Sassi, F., & Garcia, R. R. (2010). Toward a physically based gravity wave source parameterization in a general circulation model. *Journal of the Atmospheric Sciences*, *67*(1), 136–156. https://doi.org/10.1175/2009JAS3112.1

Saha, S., Moorthi, S., Wu, X., Wang, J., Nadiga, S., Tripp, P., et al. (2014). The NCEP climate forecast system version 2. *Journal of Climate*, *27*(6), 2185–2208. https://doi.org/10.1175/JCLI-D-12-00823.1

Sato, K., Tateno, S., Watanabe, S., & Kawatani, Y. (2012). Gravity wave characteristics in the Southern Hemisphere revealed by a high-resolution middle-atmosphere general circulation model. *Journal of the Atmospheric Sciences*, *69*(4), 1378–1396. https://doi.org/10.1175/JAS-D-11-0101.1

Sato, K., & Yoshiki, M. (2008). Gravity wave generation around the polar vortex in the stratosphere revealed by 3-hourly radiosonde observations at Syowa Station. *Journal of the Atmospheric Sciences*, *65*(12), 3719–3735. https://doi.org/10.1175/2008JAS2539.1

Senf, F., & Achatz, U. (2011). On the impact of middle-atmosphere thermal tides on the propagation and dissipation of gravity waves. *Journal of Geophysical Research*, *116*, D24110. https://doi.org/10.1029/2011JD015794

Sharman, R., Tebaldi, C., Wiener, G., & Wolff, J. (2006). An integrated approach to mid-and upper-level turbulence forecasting. *Weather and Forecasting*, *21*(3), 268–287. https://doi.org/10.1175/WAF924.1

Simmonds, I., Keay, K., & Tristram Bye, J. A. (2012). Identification and climatology of Southern Hemisphere mobile fronts in a modern reanalysis. *Journal of Climate*, *25*(6), 1945–1962. https://doi.org/10.1175/JCLI-D-11-00100.1

Song, I. S., & Chun, H. Y. (2008). A Lagrangian spectral parameterization of gravity wave drag induced by cumulus convection. *Journal of the Atmospheric Sciences*, *65*(4), 1204–1224. https://doi.org/10.1175/2007JAS2369.1

Song, I. S., Lee, C., Kim, J. H., Jee, G., Kim, Y. H., Choi, H. J., et al. (2017). Meteor radar observations of vertically propagating low-frequency inertia-gravity waves near the southern polar mesopause region. *Journal of Geophysical Research: Space Physics*, *122*, 4777–4800. https://doi.org/10.1002/2016JA022978

Spiga, A., Teitelbaum, H., & Zeitlin, V. (2008). Identification of the sources of inertia-gravity waves in the Andes Cordillera region. In. *Annales Geophysicae*, *26*(9), 2551–2568). Copernicus GmbH. https://doi.org/10.5194/angeo-26-2551-2008

Uccellini, L. W., & Koch, S. E. (1987). The synoptic setting and possible energy sources for mesoscale wave disturbances. *Monthly Weather Review*, *115*(3), 721–729. https://doi.org/10.1175/1520-0493(1987)115<0721:TSSAPE>2.0.CO;2

UKMO (2007). Fact sheet no. 3 – Water in the atmosphere.

Vincent, R. A., Hertzog, A., Boccara, G., & Vial, F. (2007). Quasi-Lagrangian superpressure balloon measurements of gravity-wave momentum fluxes in the polar stratosphere of both hemispheres. *Geophysical Research Letters*, *34*, L19804. https://doi.org/10.1029/2007GL031072

Wang, S., & Zhang, F. (2007). Sensitivity of mesoscale gravity waves to the baroclinicity of jet-front systems. *Monthly Weather Review*, *135*(2), 670–688. https://doi.org/10.1175/MWR3314.1

Wang, S., Zhang, F., & Snyder, C. (2009). Generation and propagation of inertia–gravity waves from vortex dipoles and jets. *Journal of the Atmospheric Sciences*, *66*(5), 1294–1314. https://doi.org/10.1175/2008JAS2830.1

Watanabe, S., Sato, K., & Takahashi, M. (2006). A general circulation model study of the orographic gravity waves over Antarctica excited by katabatic winds. *Journal of Geophysical Research*, *111*, D18104. https://doi.org/10.1029/2005JD006851

Wei, J., & Zhang, F. (2014). Mesoscale gravity waves in moist baroclinic jet–front systems. *Journal of the Atmospheric Sciences*, *71*(3), 929–952. https://doi.org/10.1175/JAS-D-13-0171.1

Wu, D. L., & Jiang, J. H. (2002). MLS observations of atmospheric gravity waves over Antarctica. *Journal of Geophysical Research*, *107*(D24), 4773. https://doi.org/10.1029/2002JD002390

Wu, D. L., Preusse, P., Eckermann, S. D., Jiang, J. H., de la Torre Juarez, M., Coy, L., & Wang, D. Y. (2006). Remote sounding of atmospheric gravity waves with satellite limb and nadir techniques. *Advances in Space Research*, *37*(12), 2269–2277. https://doi.org/10.1016/j.asr.2005.07.031

Yan, X., Arnold, N., & Remedios, J. (2010). Global observations of gravity waves from High Resolution Dynamics Limb Sounder temperature measurements: A yearlong record of temperature amplitude and vertical wavelength. *Journal of Geophysical Research*, *115*, D10113. https://doi.org/10.1029/2008JD011511

Yoo, J. H., Choi, T., Chun, H. Y., Kim, Y. H., Song, I. S., & Song, B. G. (2018). Inertia-gravity waves revealed in radiosonde data at Jang Bogo Station, Antarctica (74°37′ S, 164°13′E): 1. Characteristics, energy, and momentum flux. *Journal of Geophysical Research: Atmospheres*, *123*, 13–305. https://doi.org/10.1029/2018JD029164

Yoshiki, M., Kizu, N., & Sato, K. (2004). Energy enhancements of gravity waves in the Antarctic lower stratosphere associated with variations in the polar vortex and tropospheric disturbances. *Journal of Geophysical Research*, *109*, D23104. https://doi.org/10.1029/2004JD004870

Yuan, J., & Miller, R. L. (2002). Seasonal variation in precipitation patterns to the global ocean: An analysis of the GPCP version 2 data set. *Global Biogeochemical Cycles*, *16*(4), 1103. https://doi.org/10.1029/2001GB001458

Zhang, F. (2004). Generation of mesoscale gravity waves in upper-tropospheric jet–front systems. *Journal of the Atmospheric Sciences*, *61*(4), 440–457. https://doi.org/10.1175/1520-0469(2004)061<0440:GOMGWI>2.0.CO;2

Zhang, F., Koch, S. E., Davis, C. A., & Kaplan, M. L. (2000). A survey of unbalanced flow diagnostics and their application. *Advances in Atmospheric Sciences*, *17*(2), 165–183. https://doi.org/10.1007/s00376-000-0001-1